3

Soil–vegetation–atmosphere parameterizations

3.1 Introduction

Evolution teaches us that organisms must come to terms with their environment in order to grow and reproduce successfully. This suggests that many, if not all, successful organisms have strategies that allow them to adapt to changing environmental conditions. Unfortunately, when an organism interacts with its environment, the physical processes are rarely simple and the physiological mechanisms often are poorly understood. This is the challenge one faces when trying to incorporate vegetation into numerical models.

The atmosphere and vegetation interact in a number of different ways, and many of these need to be parameterized. The main five ways in which they interact are via the biophysical control of evapotranspiration, momentum transfer, soil moisture availability, radiation, and insulation (Sellers *et al.* 1986). The discussion of soil–vegetation–atmosphere parameterizations is organized around these five interaction types.

3.1.1 Biophysical control of evapotranspiration

Plants use photosynthetically active radiation, part of shortwave radiative energy, to combine water and carbon dioxide (CO_2) into sugars and other organic compounds. Thus, plants must allow for the transfer of CO_2 from the atmosphere to the cellular sites of photosynthesis. By doing so, plants expose their saturated tissues to the atmosphere and water loss occurs. Plants regulate the amount of CO_2 exchanged, and therefore regulate water loss, by means of valve-like structures on the leaf surface called stomates. Some plants have stomates on both sides of the leaf; others on only one side. Plants try to maximize the ratio

$$\frac{|\mathrm{CO_2\ going\ in}|}{|\mathrm{H_2O\ going\ out}|}, \tag{3.1}$$

in order to capture the CO_2 needed for photosynthesis without losing too much water. This ratio is called the water use efficiency.

Many plants conserve moisture when necessary by closing their stomates. In addition, vegetation intercepts precipitation on leaf surfaces. There also is evidence that some plants will become more efficient at conserving water as atmospheric CO_2 increases owing to the burning of fossil fuels (Eumas and Jarvis 1989; Bazzaz and Fajer 1992). Henderson-Sellers *et al.* (1995) indicate that such changes can lead to decreased evapotranspiration and increased temperatures, especially in boreal and tropical forests.

Plant roots extend into the soil for depths of up to several meters and can draw water from these depths for use in photosynthesis. The vertical distribution of plant roots can influence the seasonal cycle of transpiration (Desborough 1997) and is important to summer dryness (Desborough 1997; Milly 1997). Root-zone soil moisture is strongly correlated to the daily-maximum values of surface sensible and latent heat fluxes through the effects of the vegetation (Basara and Crawford 2002). These studies illustrate that vegetation strongly influences the latent heat flux, and hence the surface energy budget, at the Earth's surface.

The importance of variations in the surface sensible and latent heat fluxes to short-range, seasonal, and climate predictions is described at the beginning of Chapter 2. However, variations in vegetation type or land use also are important. Historical changes in land use are suggested to account for most of the observed surface warming of the past several hundred years (Chase *et al.* 2001). Adding the effects of estimated vegetation changes to climate change scenarios produces substantial regional differences in climate. Results from Feddema *et al.* (2005a, b) indicate that projected vegetation changes can produce additional warming over the Amazon region, influencing the Hadley circulation and monsoon circulations. Projected agricultural expansion in the midlatitudes produces cooling and decreases the diurnal temperature range.

Plants can be categorized into either C_3 or C_4 species based upon their method of carbon fixation, the conversion of carbon dioxide and water into organic compounds during photosynthesis. While over 95% of the plant species are C_3, the different methods of carbon fixation also influence evapotranspiration. C_3 plants have an advantage over C_4 plants in cooler climates, since the energy required to fix carbon is less for C_3 plants. C_3 plants also are more water-use efficient and nitrogen efficient than C_4 plants. Since nitrogen is often the limiting nutrient for plant growth, C_3 plants tend to grow faster. However, in very warm climates C_4 plants have an advantage, since they can store higher levels of oxygen without affecting the rate of carbon fixation

compared with C_3 plants, and thus can close their stomates during the daytime to conserve water and still produce energy.

3.1.2 Momentum transfer

Vegetation canopies are a rough surface, with larger roughness lengths implying larger surface fluxes, and also producing larger surface drag forces. As discussed in Chapter 2, most field studies of the behavior of the atmospheric surface layer, from which the log wind profile is derived, avoid rough surfaces and make their measurements in areas of relatively flat terrain with few obstacles. However, vegetation is spatially highly variable, responding to soil conditions and seed dispersion, creating patches of obstacles of varying height that influence the low-level winds. Vegetation also changes on seasonal timescales, such that its roughness varies throughout the year. In some locations, the start of monsoon rains can change the surface vegetation from near desert-like to a tropical rain forest in just a few weeks (Douglas 1993), significantly altering the surface roughness and the surface energy budget. Prolonged periods of dryness can lead to widespread wildfires, destroying vegetation over large areas. Hail-producing thunderstorms also can destroy vegetation over their paths, altering surface conditions and hence the surface energy budget, and leading to feedbacks to the atmosphere (Segele *et al.* 2005).

3.1.3 Soil moisture availability

The depth and density of the rooting zone determines the soil moisture available for evapotranspiration. Typically evaporation from bare soil occurs only through a shallow depth of soil. Once the upper soil layers become very dry they can act as a barrier to further upward moisture transport through the soil. Vegetation can overcome this barrier, since the rooting zone typically extends over a deeper layer. This ability of vegetation to tap deeper moisture sources illustrates the importance of the amount, the type, and the variability of vegetation to the latent heat flux. For example, Milly (1997) suggests that a 14% decrease in the soil volume used for plant water uptake (as caused by a decrease in plant roots) can generate the same summer dryness in midlatitudes as the doubling of atmospheric CO_2 over present levels. Conversely, a 14% increase of this same soil volume (produced by an increase in plant roots) could offset the tendency for more frequent summer dryness in a world with double the levels of CO_2. These results further underscore the important role that vegetation plays in defining the surface energy budget and its ability to influence the atmosphere over both long and short timescales.

3.1.4 Radiation

The spectral properties of leaves and the multiple reflections that occur as sunlight passes through a vegetation canopy make leaves highly absorbent in the visible wavelength interval between 0.4 and 0.72 μm, where absorption of radiation by chlorophyll in the leaves generally occurs, and moderately reflective in the near infrared region from 0.72 to 4.0 μm. Because of this, the more complex vegetation schemes (e.g., Sellers *et al.* 1986; Dai *et al.* 2003) require the computation of up to five components of incident radiation: direct photosynthetically active radiation (PAR), diffuse PAR, direct near-infrared (NIR), diffuse NIR, and diffuse infrared. These quantities are needed because the absorption and transmission coefficients of radiation interacting with vegetation are highly dependent upon the angle of the incident radiative flux.

3.1.5 Insulation

Under dense vegetation the soil surface receives less radiation and is aerodynamically sheltered, which greatly influences the soil energy budget. As one might expect, this is particularly a concern within forests. The effects of insulation generally are accounted for by alterations to the momentum transfer and radiation, so they are not discussed explicitly in the following sections.

The recognition that plants are not passive sponge-like structures, but act in ways to maximize their long-term prospects for survival, has led to the development of parameterization schemes for the effects of vegetation. These schemes generally do not allow for the development and dispersion of vegetation, at least not yet (see Pan *et al.* (2002), Sitch *et al.* (2003), Bonan *et al.* (2003), and Krinner *et al.* (2005) for examples of large-scale dynamic vegetation models), but once the type and amount of vegetation has been specified at a given location, these schemes attempt to reproduce the influences of the vegetation on the environment. Thus, the vegetation itself is not predicted, rather the interaction between the vegetation and the atmosphere. These types of schemes are commonly called soil–vegetation–atmosphere transfer schemes (SVATS) in the literature.

3.2 Describing vegetation in models

Three important vegetation parameters that are used within numerical weather models are the green vegetation fraction (σ_f), the leaf area index (LAI), and the vegetation type or class. The green vegetation fraction, also referred to as the greenness fraction or fractional vegetation cover, is the model

grid cell fraction where midday downward solar radiation is intercepted by a photosynthetically active green canopy (Chen *et al.* 1996) and it acts as the weighting factor between bare soil and canopy transpiration. This, in turn, affects surface temperature and moisture forecasts through the alteration of surface fluxes. The *LAI*, a measure of the vegetation biomass, is defined as the sum of the one-sided area of green leaves above a specified area of ground surface and it plays a major role in determining the amount of transpiration from the vegetation canopy. More leaves imply a greater amount of transpiration that is possible. Holding all other parameters constant, a larger *LAI* value produces greater canopy transpiration than a lower *LAI* value. The vegetation type specifies the dominant vegetation that covers the ground within a model grid cell. Together, the vegetation fraction, *LAI*, and vegetation type can be used to describe the state and the health of the vegetation covering the land surface.

The difficulty with these vegetation parameters is that they are nearly impossible (and prohibitively expensive!) to observe routinely from the ground. Thus, some method of observing the state of the vegetation remotely is absolutely essential. Thankfully, one measurement that is helpful in trying to calculate σ_f and *LAI* and other measures of biomass, and in defining vegetation type, is the normalized difference vegetation index (*NDVI*) (Tucker *et al.* 1984). This index was developed owing to the difference in the albedo characteristics of bare soil and vegetation-covered surfaces. The albedos of bare soils are fairly constant across the visible (red, 0.62–0.75 μm) and near-infrared (NIR, 0.75–1.4 μm) portions of the spectrum, while vegetation-covered surfaces show a dramatic increase in albedo in the NIR region when compared with the visible portions of the spectrum (Fig. 3.1). Thus, the *NDVI* is a measure of the difference between two specific wavelength bands as seen from either airplanes or satellites, and is defined as

$$NDVI = \frac{\text{NIR} - \text{red}}{\text{red} + \text{NIR}}. \tag{3.2}$$

When there is no vegetation, the albedo in the red and NIR are nearly equal and *NDVI* is approximately 0.1. When there is a lot of vegetation present, then *NDVI* is at its maximum value, approaching 0.9. When clouds are present, then the red reflectance is greater than the NIR reflectance and $NDVI < 0$.

Typically, *NDVI* is calculated from the National Oceanic and Atmospheric Administration (NOAA) polar orbiting satellites using the Advanced Very High Resolution Radiometer (AVHRR) or from the National Aeronautic and Space Administration (NASA) polar orbiting satellites using the Moderate

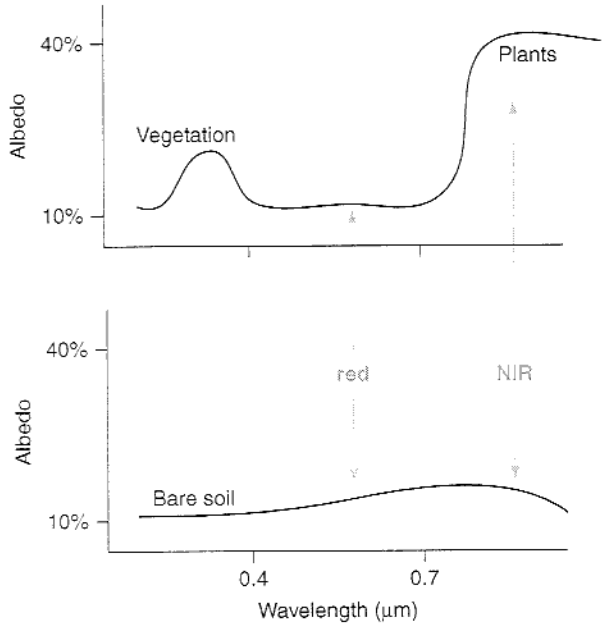

Figure 3.1. Plot of the surface reflectance (albedo) as a function of wavelength for a vegetated surface (top) and a bare soil surface (bottom). Note that the difference in the albedos between the two surfaces for the visible (red) wavelength band is small, whereas the difference in the albedos for the near-infrared (NIR) band is large.

Resolution Imaging Spectroradiometer (MODIS). While AVHRR data have a spatial resolution of ~1 km, the newer MODIS data have a spatial resolution of ~250 m. Thus, using either data source it is possible to provide vegetation information to present operational models at spatial resolutions smaller than the model grid spacing. These data sources have been used to develop global land cover mapping, the results of which are used to specify the values of σ_f and LAI in numerical models (DeFries and Townshend 1994; Loveland *et al.* 2000; Friedl *et al.* 2002). To remove the effects of clouds, a maximum value composite approach is often used in which the maximum $NDVI$ value observed over a multi-week period is determined for each grid cell and these maximum values are then used in any subsequent analyses. While there are many limitations to the use of $NDVI$ in deriving vegetation indices (Huete *et al.* 1996), it remains a very useful parameter in examining the state and evolution of vegetation.

When trying to define the health and the extent of the vegetation at the land surface, the most important parameter needed for land surface models is σ_f. Numerous studies also have shown that $NDVI$ can be related to σ_f. In particular, Chang and Wetzel (1991) indicate that $NDVI$ and σ_f are related by

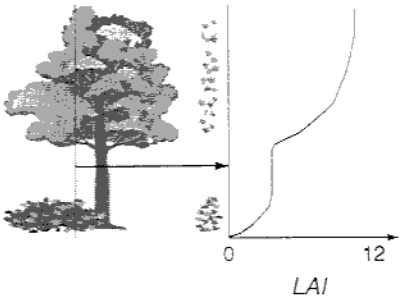

Figure 3.2. Illustration of determination of the leaf area index (LAI) from the surface to the top of the canopy. LAI is the total area of one side of all the leaves in a canopy compared to a unit surface area.

$$\sigma_f = \begin{cases} 1.5(NDVI - 0.1). & NDVI \leq 0.547. \\ 3.2(NDVI) - 1.08. & NDVI > 0.547. \end{cases} \tag{3.3}$$

which yields a linear relationship between $NDVI$ and σ_f with two slightly different regimes depending upon the value of $NDVI$. Of course, other formulas for relating $NDVI$ to σ_f are available (e.g., Carlson and Ripley 1997; Gutman and Ignatov 1998) and their coefficients depend strongly upon the spatial resolution of the $NDVI$ used in their development.

The other important aspect of the vegetation that needs to be known is some measure of the total vegetation biomass as determined using the LAI (Fig. 3.2). Typical values of LAI vary from 8 for forests, 7 for a mature corn crop, 4 for a mature wheat crop, and 0.5–2 for grasses. Plants with very clumped leaves can have LAI values above 10 and approaching 15. However, LAI is highly variable and can change from vegetation type to vegetation type and within a given year.

Numerous studies also have shown that the value of $NDVI$ can be related, albeit imperfectly, to LAI. This is seen by examining the calculated values of $NDVI$ versus field measurements of LAI, which yields a curve that slowly asymptotes to the maximum $NDVI$ value as LAI increases (Fig. 3.3). The idea behind the calculation of LAI from $NDVI$ is that if the maximum and minimum $NDVI$ values for a given location can be determined using a multi-year time series, and if the maximum value of LAI attained at this same point is known based upon the vegetation type, then a linear relation between the value of $NDVI$ to the expected LAI can be constructed. This approach leads to formulas such as that developed by Yin and Williams (1997) in which

$$LAI_i = LAI_{max} \frac{(NDVI_i - NDVI_{min})}{(NDVI_{max} - NDVI_{min})}. \tag{3.4}$$

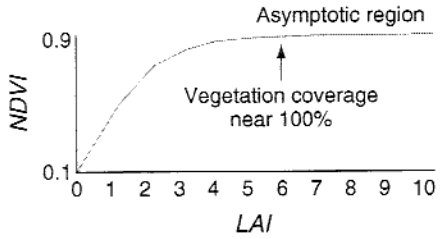

Figure 3.3. Curve typically found when plotting values of *NDVI* versus *LAI*. Saturation is reached when *LAI* increases past 3 or 4 as the value of *NDVI* is effectively constant while *LAI* continues to increase. Adapted from Sellers (1987).

Here i refers to the day of interest, the maximum and minimum values of *NDVI* are calculated over many years worth of data, and the value of LAI_{max} is determined from a vegetation database. While not a perfect relationship, this does provide useful and helpful information on the variations of the vegetation biomass for some midlatitude regions where the *LAI* is zero during the cold season. As seen in (3.4), *LAI* is zero when $NDVI_i$ equals $NDVI_{min}$. This is a reasonable relationship for midlatitude deciduous forests and grasslands, but does not apply for coniferous forests or tropical regions. For these areas *LAI* is almost never zero and a constant is probably needed on the right-hand side of (3.4) along with a corresponding modification to the value of LAI_{max}. Carlson and Ripley (1997) indicate that the relationship between *NDVI* and *LAI* is only valid up to values of *LAI* between 3 and 4. Beyond a *LAI* value of 4, *NDVI* is effectively constant.

Many models use the 5 year climatology of σ_f derived from 1 km AVHRR data by Gutman and Ignatov (1998) at 0.15° resolution. Some models use a constant value for *LAI* over the entire model grid, while others use values for *LAI* that are derived from satellite data (Buermann *et al.* 2001; Mitchell *et al.* 2004). These values of σ_f and *LAI* generally are provided once a month, and the daily values are interpolated from these monthly mean values.

However, it is clear that vegetation is greatly affected by the amount of precipitation, sunshine, and temperature and responds to changes in any of these inputs relatively rapidly. Differences between 14 day composite maximum values of σ_f compared to the multi-year mean of Gutman and Ignatov (1998) are calculated by Kurkowski *et al.* (2003) and are substantial (Fig. 3.4). Differences between the assumed model values of σ_f and the near real-time observed values exceed 30% at some locations. Thus, it is important to consider the initial data that go into the model in addition to the parameterization schemes used. Buermann *et al.* (2001) indicate that values of *LAI* also change significantly from year to year and that these changes are important to the partitioning of the sensible and latent heat fluxes.

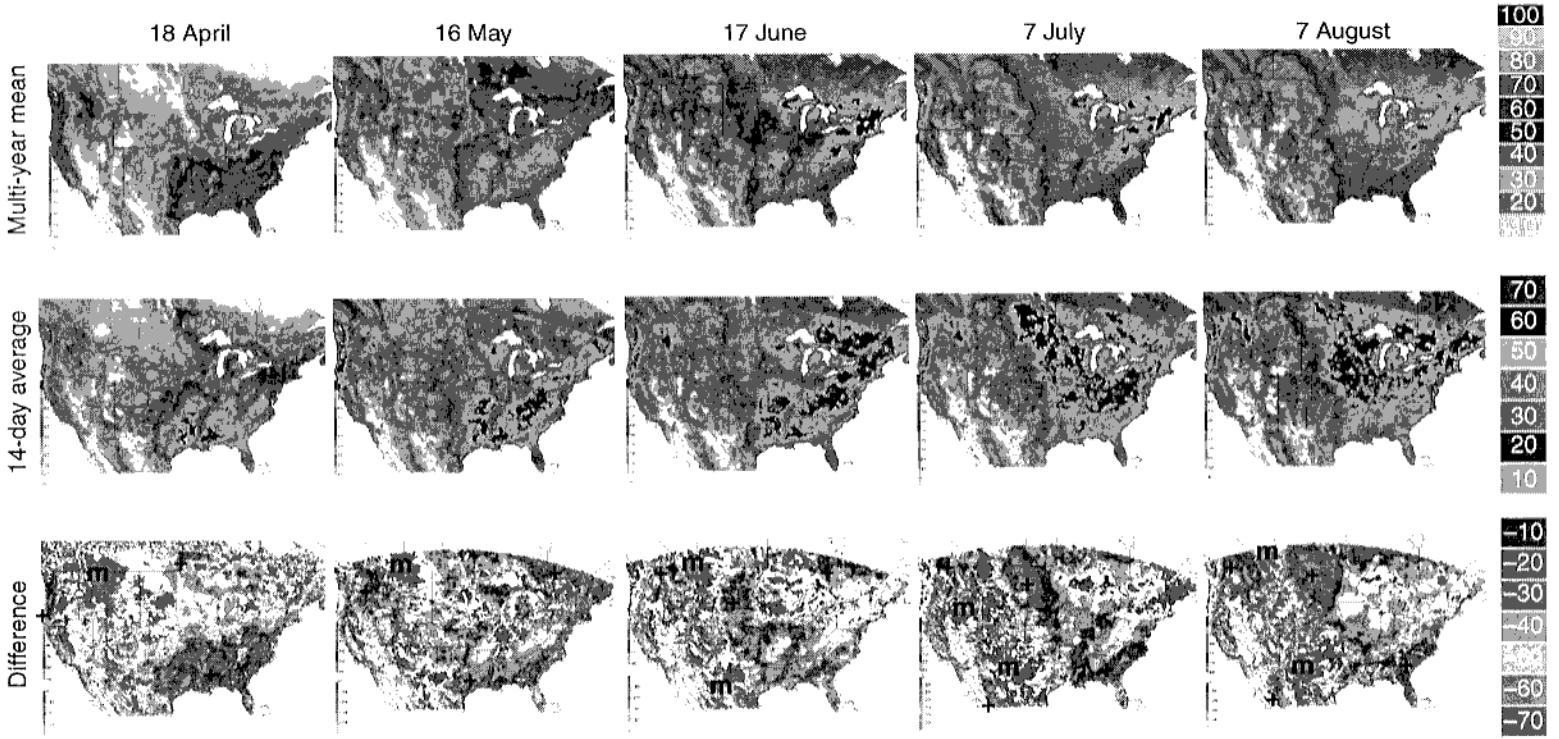

Figure 3.4. Multi-year mean values of σ_f from Gutman and Ignatov (1998) as implemented in the Eta model (top), near real-time 14 day composite maximum values of σ_f (middle), and the difference (real-time minus multi-year mean, bottom) for 5 days during the warm season of 2001. Scale for the σ_f values shown in the upper right, with the scale for the difference field in the lower right. The symbols + and m in the bottom panel denote the larger, cohesive areas with positive and negative differences, respectively. Note that the southeastern USA in April is much greener in 2001 than in the multi-year mean, as is the high plains region in July and August. The value of the real-time σ_f over the west is generally less than the multi-year mean, although the monsoon region of western Mexico shows up as greening up earlier than the multi-year mean in July and August. From Kurkowski *et al.* (2003).

Vegetation type or class databases are generally derived from polar-orbiting satellite data. Again, the 1 km resolution NOAA AVHRR instrument has provided most of the data used by the United States Geological Survey to create several 1 km resolution global land cover categorizations. One is a simple biosphere model vegetation categorization that consists of 16 land cover classes, while another consists of a 25 category land cover classification (Loveland *et al.* 2000). Hansen *et al.* (2000) also have developed a global 1 km land cover classification (Fig. 3.5).

These vegetation type categorizations are based upon the phenology of the vegetation as observed using composite 14 day, 1 km pixel values of *NDVI*. In these composites, the maximum value of *NDVI* observed over the 14 day period is assigned to each pixel. This approach greatly reduces the effects of clouds, since clouds generally produce negative values of *NDVI*. Once the 14 day composites are available throughout an entire year, time series of *NDVI* are constructed for each 1 km pixel and depict the annual progression of the vegetation from spring greenup, when the vegetation develops leaves and crops begin to emerge, to fall retrogression, when vegetation drops its leaves and crops are harvested. Distinctive signatures in the *NDVI* time series are found for different vegetation classes (Fig. 3.6), which allows for the vegetation class to be assigned without expensive and time-consuming ground surveys. However, the USGS also conducts ground surveys in different regions to verify the satellite-based class assignments. While satellite-based techniques require less time and effort than ground surveys, they are still very time consuming and are not done every year. Many of the land surface models presently use vegetation classifications based upon satellite data that are nearly a decade old.

Another challenge found when using vegetation class databases is that while there are a large number of vegetation categories (>200) that have been observed and documented (see Loveland *et al.* 2000), a total of fewer than 30 different vegetation types are defined for use in land surface models. This means that similar, yet different, vegetation types are aggregated into a single category. Xue *et al.* (1996) and McPherson and Stensrud (2005) show that use of so few vegetation categories can lead to problems with the resulting surface fluxes, since the behavior of individual vegetation types that are grouped together into a single category can be vastly different. However, it is very difficult to specify the vegetation parameters needed by soil–vegetation–atmosphere parameterization schemes for a vast number of vegetation types, and it is unclear whether the effort required to define these parameters will be repaid by substantially improved surface flux predictions.

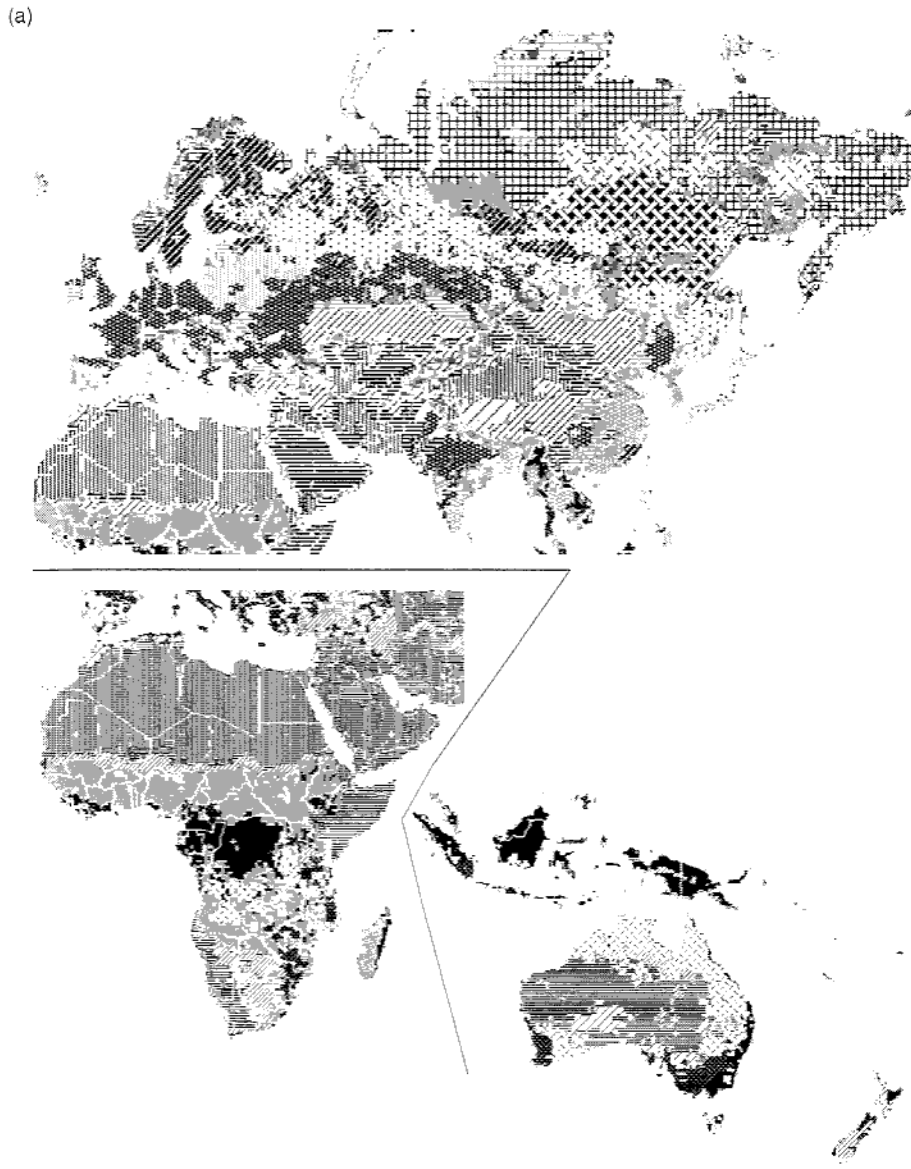

Figure 3.5. Predominant vegetation type in each 60 km grid cell over the *globe, with urban = 1, dryland crop pasture = 2, irrigated crop pasture = 3,* mixed dryland and irrigated crop pasture = 4, cropland and grassland mosaic = 5, cropland and woodland mosaic = 6, grassland = 7, shrubland = 8, mixed shrubland and grassland = 9, savanna = 10, deciduous broadleaf = 11, deciduous needleleaf = 12, evergreen broadleaf = 13, evergreen needleleaf = 14, mixed forest = 15, water and ice = 16, herbaceous wetland = 17, wooded wetland = 18, barren or sparse vegetation = 19, herbaceous tundra = 20, wooden tundra = 21, mixed tundra = 22, and bare ground tundra = 23. A color version of a similar global vegetation mapping can be found in Rodell *et al.* (2004).

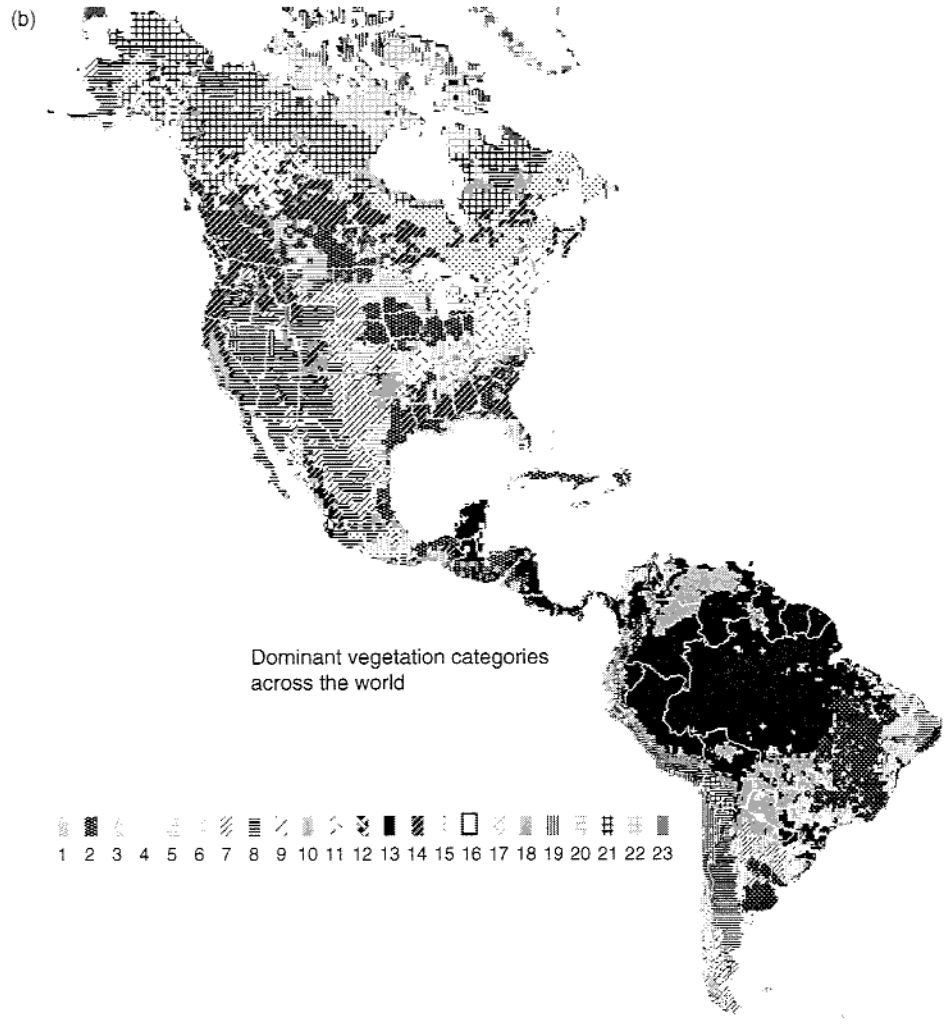

Figure 3.5. (cont.)

Land surface parameterizations often divide vegetation into two main categories: trees or shrubs, and groundcover. Some land surface parameterizations represent only the dominant vegetation type within the grid cell, while others represent perhaps the first few dominant vegetation types. However, regardless of which approach is taken, there is little doubt that each 1 km pixel observed by the AVHRR instrument has a number of different vegetation types within it. The vegetation classification applies most appropriately to the dominant vegetation class within each pixel. The lack of ability to use the satellite-derived vegetation class information fully is an area in which progress can be made.

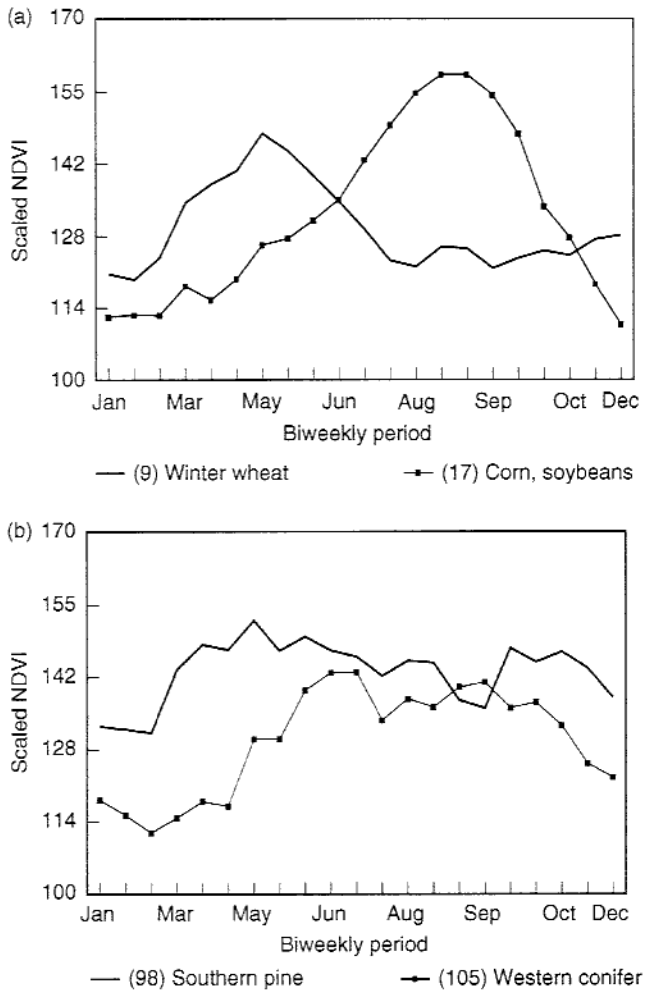

Figure 3.6. *NDVI* time series during 1990 for selected seasonal land-cover regions. Winter wheat and corn–soybeans are shown in the top panel, while southern pine and western conifer are shown in the bottom panel. From Loveland *et al.* (1995).

3.3 Describing soils in models

Worldwide information on soil type is derived from the Soil Map of the World, produced during the 1970s by the Food and Agriculture Organization (FAO) of the United Nations Educational, Scientific, and Cultural Organization (UNESCO). The original map is contained within 10 print volumes at a scale of 1:5 000 000 (1 cm on the map equals 50 km). The map is based upon data compiled over a 15 year period using input from field surveys and map collections. Roughly 11 000 individual soil maps were reviewed to produce the

worldwide map and these individual maps varied widely in reliability, detail, scale, and the methodologies used (Zobler 1986). At the time of map creation, only Europe had systematic soil surveys for over half of the land area; the other continents on average had systematic soil surveys for only 16% of the total land area (Gardiner 1982). Approximately 40% of the world had only general information surveys available for soil type.

The original printed map volumes were digitized by Zobler (1986) into 1° latitude by 1° longitude grid cells. Transparent overlaps were used to define the grid cells and the dominant soil type, soil texture, and the slope for each cell were determined manually if over 50% of the grid cell area was land. The soil texture information represents the relative proportions of clay (2 μm or smaller particle size), silt (2–50 μm particle size), and sand (50–200 μm particle size) using three general classes: coarse texture with less than 18% clay and more than 65% sand, medium texture with less than 35% clay and less than 65% sand, and fine texture with more than 35% clay. These three classes also could be combined, such that a total of seven textural classes are seen on the printed map pages.

The soil texture information contained in the map volumes is used by Zobler (1986) to specify a soil texture class for each grid cell based upon the commonly used United States Department of Agriculture (USDA) soil textural triangle (Fig. 3.7). There are 12 soil texture categories in this taxonomy that are

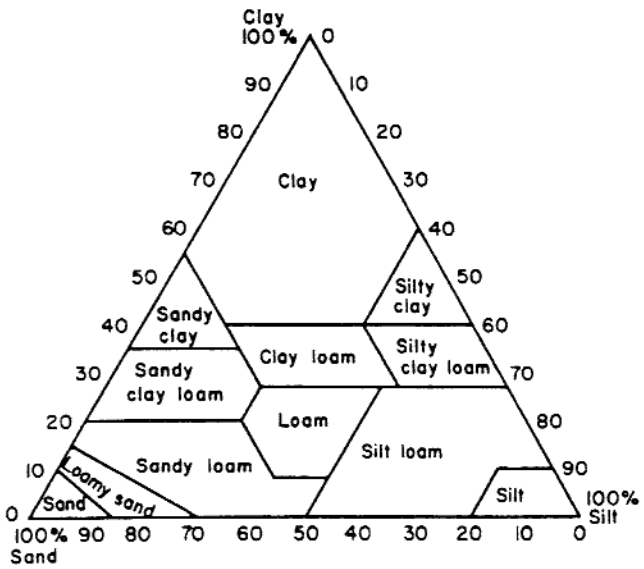

Figure 3.7. The USDA soil texture triangle, showing the percent by weight of clay, silt, and sand particles. The 12 soil categories are outlined, and indicate the range of composition of the soils within each of the classes. Other classifications of soil are available (see Marshall *et al.* 1996). From Cosby *et al.* (1984).

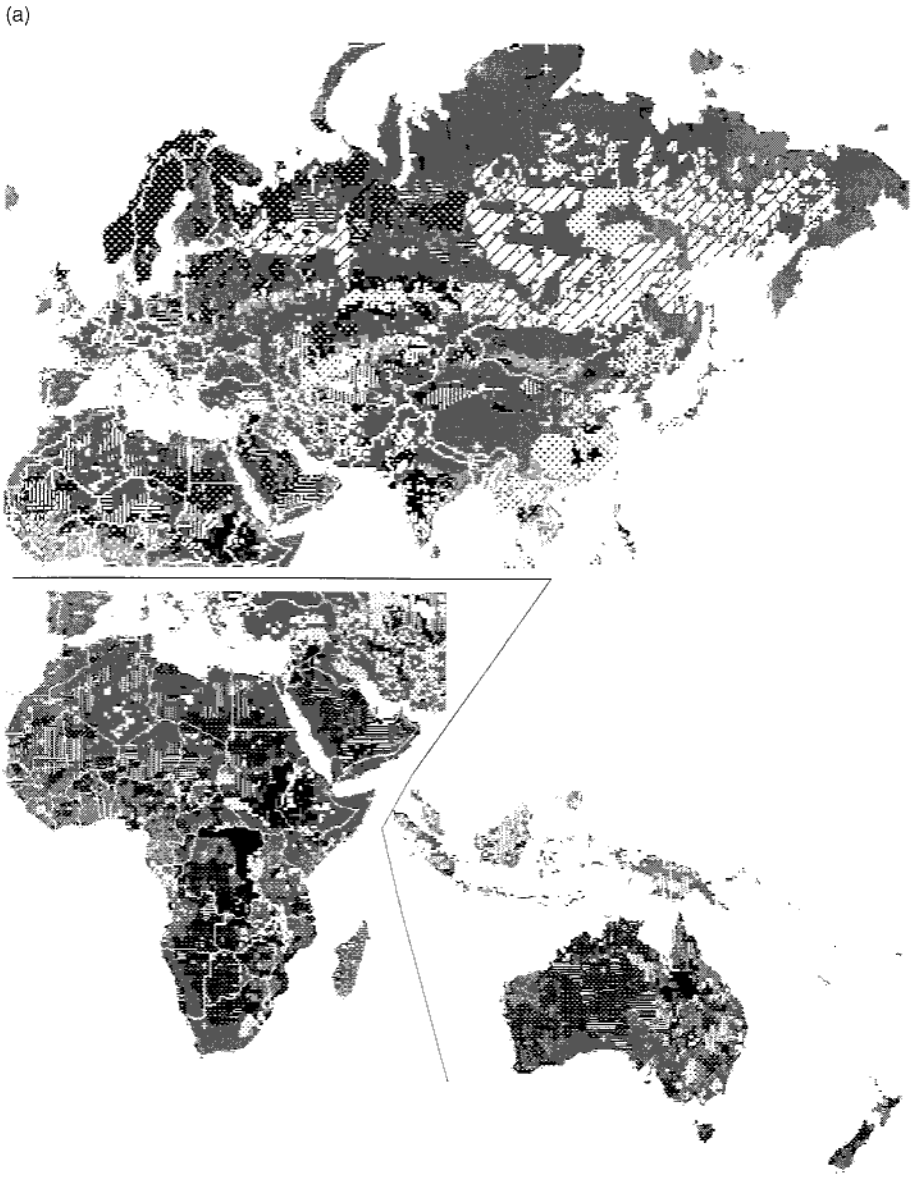

Figure 3.8. Global soil texture classes in each 60 km grid cell with sand = 1, loamy sand = 2, sandy loam = 3, silt loam = 4, silt = 5, loam = 6, sandy clay loam = 7, silty clay loam = 8, clay loam = 9, sandy clay = 10, silty clay = 11, clay = 12, organic materials = 13, bedrock = 14, and other = 15. See Rodell *et al.* (2004) for a color figure of global soil texture from a slightly different database.

separated based upon the relative amounts by weight of clay, silt, and sand in the soil. These data are now available in digital form and are often used to specify the soil type and texture for use in numerical weather prediction models with some soil data interpolated down to every 30 seconds. For example,

(b)

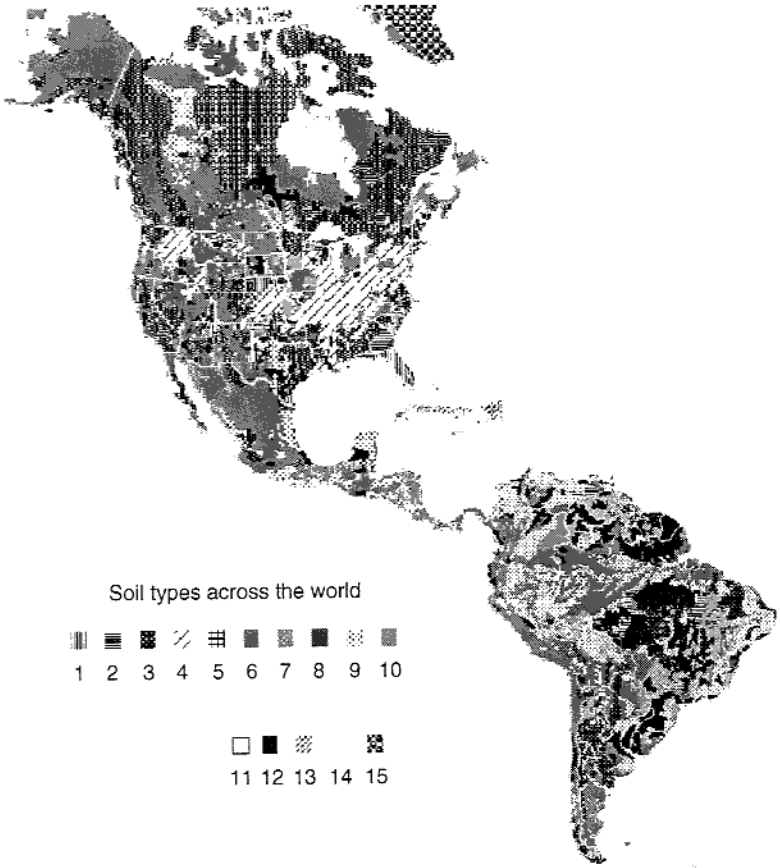

Figure 3.8. (cont.)

Reynolds *et al.* (2000) provide a 5 min, 16-category, two-layer soil texture database for the entire globe (Fig. 3.8). However, the detail and data quality of the original maps used to generate these types of databases has not changed and users should be aware of these limitations.

Information from the FAO Soil Map of the World also has been used to derive soil profiles and to estimate the water holding capacity of the soils (Webb *et al.* 1993). In addition, an international effort is underway to update the Soil Map of the World. The Soil and Terrain (SOTER) project is a joint effort of many groups to produce an updated, generalized map of the world soil resources.

Since the creation of the FAO Soil Map of the World many other soil surveys have been conducted and their data made available in digital form. In the USA, each of the individual 50 states have conducted detailed soil surveys down to a depth of 203.2 cm (80 in) or until bedrock is reached. If needed, soil samples were taken every 5.7 acres ($\sim$362 m^2) or often enough

to verify a geomorphic landscape and draw out common soil areas. These data were combined into a State Soil Geographic (STATSGO) database by the USDA in which the more detailed soil surveys were transected and sampled to represent the soil information well on a regional scale. STATSGO data are available down to 30 second resolution, or grid cells of roughly 0.9 km in size and can be ingested easily into geographic information systems. Miller and White (1998) report on a 1 km, multi-layer 16-category (12 USDA soil texture classes plus organic material, water, bedrock, and other) soil texture database for 11 soil layers down to a 2 m depth that is available over the USA.

It also is important to consider how soil surveys are conducted. Some soil surveys quantify the proportion of clay, silt, and sand using a particle size analysis to obtain a very precise determination of the relative amounts of each particle type. However, the 12 soil texture classes marked off in Fig. 3.7 show the range of composition of the soils that represent each of the textural classes. It is clear that the variability in soil composition within individual soil classes often exceeds the variability in soil composition between soil classes. In addition, as discussed by Marshall *et al.* (1996), soil classification in the field is sometimes determined by working moistened soil between the fingers to sense the coarseness or fineness of the non-clay particles and to sense the strength and plasticity imparted by the clay particles. Thus, when the particle size distributions of a soil sample are plotted on the texture triangle, it is possible that the texture class into which the soil sample falls does not correspond to the texture class given in the field. Marshall *et al.* (1996) mention studies in which only half of the field texture class determinations fall within the same texture class when determined using the particle distributions. This occurs owing to the presence of clay minerals, organic matter, and cementing agents that strongly influence the field determination of texture. Field determinations of soil texture correspond to the particle size analysis in an average way, but not on a one-to-one basis. These uncertainties in the quality of the soil surveys and the range of soil compositions within a single soil textural class suggest that defining the soil conditions accurately at any specific location is difficult.

Many uncertainties arise when using the soil textures provided by global databases. In addition, many land surface schemes ignore the change in soil texture as a function of soil depth, instead assuming a constant texture. While a soil texture database is likely to provide a reasonable picture of soil texture and its variation over broad regions, it is not at all certain or guaranteed that the soil texture observed at a given location on the ground would agree with that specified from a global soil texture database. Other challenges are found when converting from the original soil database format to one that has a uniform grid cell (which is most convenient for meteorological models) as discussed by Miller and White (1998).

3.4 Biophysical control of evapotranspiration

The parameterization of evapotranspiration in most land surface schemes is divided into contributions from the bare soil, vegetation, and water on the canopy. Thus, we typically have

$$Q_E = Q_{EB} + Q_{EV} + Q_{EW}, \tag{3.5}$$

where Q_{EB} is bare soil evaporation, Q_{EV} is transpiration from the vegetation, and Q_{EW} is evaporation of liquid water from leaves on a wet canopy. The formulas for Q_{EB} and Q_{EW} are relatively straightforward and there is not as much difference in them among the various models. Thus, we examine these terms first and save Q_{EV} for last, since the parameterization of this term has the most variability from scheme to scheme.

3.4.1 Bare soil evaporation

The evaporation from bare soil is often parameterized as a fraction of the potential evaporation, where this fraction depends upon the value of the near-surface soil moisture. Thus, a number of schemes (e.g., Chen and Dudhia 2001) define

$$Q_{EB} = (1 - \sigma_f)\beta E_p, \tag{3.6}$$

where E_p is the potential evaporation and

$$\beta = \frac{\Theta_1 - \Theta_w}{\Theta_{fc} - \Theta_w}. \tag{3.7}$$

Here Θ_1 is the volumetric water content within the topmost soil layer, Θ_{fc} is the volumetric water content field capacity, and Θ_w is the wilting point (the volumetric water content at which plants can no longer bring water out of the soil). These two values depend upon the soil type and are determined from a soil database. Ek *et al.* (2003) indicate that this leads to evaporation falling off too slowly as soil moisture declines, and recommend a modified equation in which β is replaced by β^2. This modification may be related to the process of rapid soil drying as described by Santanello and Carlson (2001).

Another approach to parameterizing the bare soil evaporation is seen in Noilhan and Planton (1989), Mahfouf (1991), and Viterbo and Beljaars (1995), where they define

$$Q_{EB} = (1 - \sigma_f)\rho_a L_v \frac{(h_u q_s(T_g) - q_a)}{r_a}, \tag{3.8}$$

in which

$$h_u = \begin{cases} \frac{1}{2}\left[1 - \cos\left(\frac{\Theta\pi}{1.6\Theta_{fc}}\right)\right], & \Theta < \Theta_{fc}, \\ 1. & \Theta \geq \Theta_{fc}. \end{cases} \tag{3.9}$$

Here the dependence upon soil moisture is multiplied by $q_s(T_g)$, instead of by E_p as in (3.6). Thus, the h_u parameter is used to approximate the surface relative humidity, in contrast to β in (3.6) which is used to approximate the fraction of potential evaporation. It is unclear which approach is more realistic, and although these two methods generally behave in a similar fashion, they also produce very different answers.

It also is important to point out at this juncture that there are many ways to calculate the resistance r_a. For example, Viterbo and Beljaars (1995) use the results of Beljaars and Holtslag (1991) to define their expression for resistance, which uses a wind speed that incorporates an estimate of the vertical motion as well as the horizontal wind. They also use a transfer coefficient that depends upon the sensible heat flux. In general, the forms of the resistances closely resemble those defined in Chapter 2, but the devil is always in the detail.

If we focus only upon the potential difference (Δq) and the β and h_u parameters, ignoring the different contributions from resistances, and set $\Theta_w = 0.10$ and $\Theta_{fc} = 0.38$, then the β approach produces a linear increase in Δq whereas the h_u approach produces a more gradual, non-constant increase in Δq (see Fig. 3.9). One of the important differences between these three approaches is that Δq remains positive below $\Theta = 0.10$ from the h_u approach, whereas the β

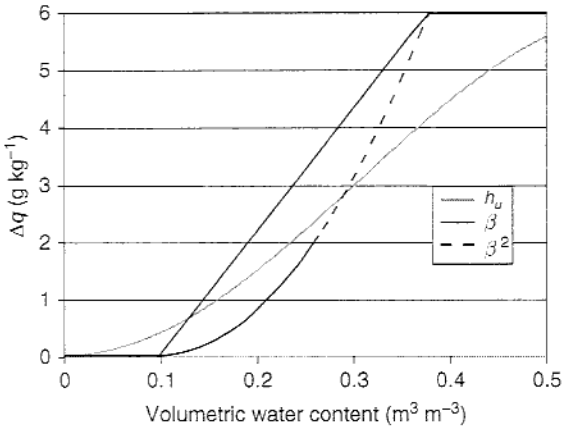

Figure 3.9. Values of Δq versus Θ for the expressions $[h_u q_s(T_g) - q_a]$ (gray line), $[\beta(q_s(T_g) - q_a)]$ (black line), and $[\beta^2(q_s(T_g) - q_a)]$ (dashed line), assuming that T_g and q_a are constant and the same for all expressions. It is assumed that $q_s(T_g) - q_a = 6\,\mathrm{g\,kg^{-1}}$, $\Theta_w = 0.10$ and $\Theta_{fc} = 0.38$ for this example.

approach allows no evaporation below the wilting point. In addition, the β approach reaches the potential evaporation at field capacity, while the h_u approach fails to reach the potential evaporation over the range of volumetric water contents evaluated. Thus, while evaporation increases in both schemes as the volumetric water content increases, the value for which evaporation first becomes non-zero and the actual values of evaporation can be quite different from the two schemes for identical values of soil moisture.

A third approach to bare soil evaporation is taken by Chen *et al.* (1996), in which they define

$$Q_{EB} = (1 - \sigma_f) \min\left(\left[-D_w \frac{\partial \Theta}{\partial z} - \kappa_w \right]_{z_1}, E_p \right), \tag{3.10}$$

where D_w and κ_w are the soil water diffusivity and thermal conductivity, respectively, and are evaluated for the topmost soil layer z_1. When the soil is moist, evaporation occurs at the potential rate E_p, but when the soil is drier evaporation only occurs at the rate by which the topmost soil layer can transfer water upward from lower soil levels. This approach certainly appears to be the most physical, in that evaporation only occurs at the rate by which moisture can be supplied by the upward water transfer in the soil. However, errors in this water transfer rate then directly influence the amount of latent heat flux, whereas in the other approaches the effect is more indirect. In addition, it is possible that the number of vertical soil levels influences the water transfer rate, so the choice of these levels is likely to influence the values of latent heat flux.

The potential evaporation E_p as specified in two of the approaches to calculating Q_{EB} is calculated using a Penman–Monteith formulation from Mahrt and Ek (1984). This approach typically avoids overestimating E_p as is seen in the more traditional approach that uses $q_s(T_g)$ in the formulation. Mahrt and Ek (1984) derive a slightly modified form of the Penman–Monteith equation, and use an exchange coefficient following the results of Louis (1979) and Louis *et al.* (1982) that depends upon the Richardson number (Ri), arriving at

$$E_p = \frac{\Delta(R_{net} - Q_G)}{1 + \Delta} + \frac{\rho L_v (q_s(T_a) - q_a)}{(1 + \Delta) r_a}, \tag{3.11}$$

where Δ is related to the change of saturation vapor pressure with respect to temperature and is defined as

$$\Delta = \frac{0.622}{p} \frac{L_v}{c_p} \frac{de_s(T)}{dT}, \tag{3.12}$$

and so is not assumed to be a constant as in the original Penman–Monteith derivation, $r_a = 1/(C_q u)$, u is the surface wind speed, and for the unstable case ($Ri < 0$) they use

$$C_q = \left[\frac{k}{\ln\left(\frac{z+z_0}{z_0}\right)}\right]^2 \left(1 - \frac{15Ri}{1 + C\sqrt{-Ri}}\right), \tag{3.13}$$

with

$$C = \frac{75k^2\left(\frac{z+z_0}{z_0}\right)^{1/2}}{\left[\ln\left(\frac{z+z_0}{z_0}\right)\right]^2}, \tag{3.14}$$

and for the stable case ($Ri > 0$),

$$C_q = \left[\frac{k}{\ln\left(\frac{z+z_0}{z_0}\right)}\right]^2 \left[(1+15Ri)(1+5Ri)^{1/2}\right]^{-1}. \tag{3.15}$$

Here the Richardson number is defined as

$$Ri = \frac{g}{\theta}\frac{(\theta - \theta_{sfc})z}{u^2}, \tag{3.16}$$

where z is the height of the observation (θ and u), and θ_{sfc} is the potential temperature of the air at the lowest reference level. They find that this formulation of E_p is very sensitive to the diurnal variation of C_q, owing to the dependence upon Ri, and can lead to a factor of 2 difference between the formulations with and without this diurnal variation on days with moderate instability.

If we recall the definition of resistance to sensible heat flux from Chapter 2, and use our knowledge of the log wind profile under neutral conditions, then we can develop a modified definition of resistance where

$$r_H = \left(\frac{\ln\left(\frac{z+z_0}{z_0}\right)}{k}\right)^2 \frac{1}{\bar{u}}, \tag{3.17}$$

which is basically the inverse of the first term on the right-hand side of the definition of C_q in (3.13) and (3.15) multiplied by $1/\bar{u}$. Thus, the resistance used in the Mahrt and Ek (1984) formulation of potential evaporation is

basically the same resistance derived previously in Chapter 2, but multiplied by an expression that depends upon the Richardson number. The use of the Richardson number is yet another approach to account for non-neutral conditions and the effects of atmospheric stability on the resistance calculations.

The previous formulations for bare soil evaporation are from land surface parameterizations that have a single combined bare soil and vegetation layer. However, there are schemes that use separate equations for the ground surface and the canopy layer, and one such scheme is the simple biosphere parameterization (Sellers *et al.* 1986). In their formulation, the evaporation from the bare soil is expressed as

$$Q_{EB} = \frac{\rho c_p \left[e_s(T_g) - e_a\right]}{\gamma} \left[\sigma_f \left(\frac{\sigma_w}{r_d} + \frac{1-\sigma_w}{r_d + r_g}\right) + \frac{(1-\sigma_f)(f_h e_s(T_g) - e_a)}{(r_s + r_d)(e_s(T_g) - e_a)}\right], \tag{3.18}$$

where r_d is the resistance between the ground and the canopy level, r_g is the bulk resistance of the groundcover, r_s is the bare soil surface resistance, σ_w is the wetted fraction of groundcover, and f_h is the relative humidity of the air at the soil surface. Definitions for the various resistances are found in Sellers *et al.* (1986). The main point is that, while the processes included in this expression are much greater than in the earlier bare soil evaporation equations, the number of parameters needed also has increased. Several of the resistances are expressed simply in terms of a surface-dependent constant multiplied by the near-surface wind speed. It is not clear if the added complexity provides additional accuracy to the calculations.

3.4.2 Canopy water evaporation

The parameterization for the evaporation of liquid water from on top of the leaves on a wet canopy is somewhat more consistent across the literature. Many of the formulations follow Noilhan and Planton (1989) and Jacquemin and Noilhan (1990) who define

$$Q_{EW} = \sigma_f \left(\frac{W_c}{S}\right)^n E_p, \tag{3.19}$$

where W_c is the intercepted canopy liquid water content, S is the maximum intercepted canopy water capacity (typically 0.5–2 mm), and $n = 0.5$. Mahfouf *et al.* (1995) define the value of S as proportional to LAI, while other approaches relate it to the vegetation type. The intercepted canopy water budget is determined by

$$\frac{\partial W_c}{\partial t} = \sigma_f P - D - \frac{Q_{EW}}{\rho_w L_v}, \tag{3.20}$$

where P is the precipitation rate, D is the rate of precipitation that drips off the canopy leaves and falls onto the ground, and ρ_w is the density of water. These schemes typically account for both precipitation and dewfall on the canopy and follow the approach outlined by Rutter *et al.* (1971, 1975). For schemes with a separate canopy temperature equation, interception and evaporation of water from groundcover also may be included (Sellers *et al.* 1986).

A slightly different expression is used by Viterbo and Beljaars (1995), where the potential evaporation is defined using the ground temperature, instead of the Penman–Monteith formulation, and the fraction of the model grid cell covered by the interception reservoir is defined as

$$C_l = \min\left(1, \frac{W_c}{S}\right), \tag{3.21}$$

where

$$S = \left[\sigma_f LAI + (1 - \sigma_f)\right] S_{max}, \tag{3.22}$$

and S_{max} is a constant that indicates the maximum amount of water on a single leaf or as a thin film over the ground (chosen as 0.0002 m in Viterbo and Beljaars (1995)). Thus, their final expression for canopy water evaporation is

$$Q_{EW} = C_l E_p. \tag{3.23}$$

They argue that, while the use of the $n = 0.5$ provides for a faster depletion of canopy water and that using $n = 1$ may mean that the canopy water never entirely disappears, they find no difficulties with using $n = 1$ in their formulation.

3.4.3 Transpiration from vegetation

The parameterization of the vegetation transpiration is accomplished using several approaches. Most of the canopy models described below can be called big-leaf models since they map the properties of the entire vegetation canopy onto a single leaf to calculate the transpiration. In addition, these canopy models generally only calculate the transpiration and do not worry about carbon exchange or photosynthesis rates. For example, Pan and Mahrt (1987) propose that

$$Q_{EV} = E_p k_v \sigma_f \left[\frac{z_1}{z_2} g(\Theta_1) + \frac{(z_2 - z_1)}{z_2} g(\Theta_2)\right]\left[1 - \left(\frac{W_c}{S}\right)^n\right], \tag{3.24}$$

where z_1 and z_2 are the soil layer depths, k_v is the plant resistance factor or plant coefficient (typically assumed to be 1, although it can be specified as a function of plant type), E_p is calculated as in Mahrt and Ek (1984) using a modified Penman–Monteith approach, and g is defined as

$$g(\Theta) = \begin{cases} 1, & \Theta > \Theta_{ref}, \\ \dfrac{\Theta - \Theta_w}{\Theta_{ref} - \Theta_w}, & \Theta_w \leq \Theta \leq \Theta_{ref}, \\ 0, & \Theta \leq \Theta_w, \end{cases} \tag{3.25}$$

where Θ_{ref} is assumed to be 0.25 in Pan and Mahrt (1987). Smirnova *et al.* (1997) use the same approach. This approximation draws water out of the soil layers in which the roots are assumed to exist in proportion to their depths and the volumetric water content of each layer. It also is assumed that the water on the canopy has to evaporate before maximum evaporation from the vegetation is reached. Desborough (1997) highlights how changes in surface root fraction influence transpiration, while Zeng (2001) develops a global vegetation root distribution for the most widely used land cover classifications.

Noilhan and Planton (1989) use a slightly different approach, and express the canopy evaporation as

$$Q_{EV} = \sigma_f \rho_a \frac{L_v[q_s(T_g) - q_a]}{r_a + r_c} \left[1 - \left(\frac{W_c}{S}\right)^{2/3}\right], \tag{3.26}$$

where $r_a = 1/(C_h u)$, C_h is a transfer coefficient depending upon the thermal stability of the atmosphere, and the canopy resistance is defined as

$$r_c = \frac{r_{c\,min}}{LAI \cdot F_1 F_2 F_3 F_4}. \tag{3.27}$$

The F-factors account for the effects of solar radiation, vapor pressure deficit, air temperature and soil moisture in the calculation of canopy resistance (Noilhan and Planton 1989). The F_1-factor is based upon the studies of Dickinson (1984) and Sellers *et al.* (1986) and is defined as

$$F_1 = \frac{f + (r_{c\,min}/r_{c\,max})}{1 + f}, \tag{3.28}$$

with

$$f = 0.55 \frac{Q_S}{Q_{GL}} \frac{2}{LAI}, \tag{3.29}$$

and where $r_{c\,min}$ is the minimum stomatal resistance, $r_{c\,max}$ is the maximum stomatal resistance (typically set to 5000 s m^{-1} as in Dickinson 1983), Q_S is the incoming solar radiation that reaches the surface, and Q_{GL} is a scaling parameter that typically depends upon the vegetation type and varies from 30 W m^{-2} for trees to 100 W m^{-2} for crops (Jacquemin and Noilhan 1990). The minimum stomatal resistance also depends upon the vegetation type, highlighting the importance of our knowledge of the underlying vegetation to the calculations of transpiration. As one can see from (3.28), F_1 is less than 1 and decreases as Q_S decreases. Thus, owing to the influence of F_1 only, r_c is likely to reach its minimum value at local noon when Q_S is largest and reaches its maximum value at sunrise and sunset, and retains this value throughout the night. This diurnal evolution of r_c agrees well with observations of canopy resistance summarized in Monteith and Unsworth (1990).

The F_2-factor represents the effects of the vapor pressure deficit on the canopy resistance, and is expressed in Noilhan and Planton (1989) as

$$F_2 = 1 - g\left[e_s(T_g) - e_a\right], \tag{3.30}$$

where g is a vegetation-dependent empirical parameter. Using a different formulation, Jacquemin and Noilhan (1990), based upon the studies of Jarvis (1976) and Avissar *et al.* (1985), define F_2 as

$$F_2 = \frac{1}{1 + \alpha[q_s(T_a) - q_a]}, \tag{3.31}$$

where α is a vegetation-dependent parameter that typically varies from 36 to 60. Under typical conditions, F_2 varies from 0.5 to 1.0, with the smaller values occurring for larger vapor pressure deficits. Thus, r_c increases as the vapor pressure deficit increases, and represents the stomatal response to the environmental conditions.

The influence of the ambient temperature upon canopy resistance is taken from Dickinson (1984), such that F_3 is expressed as

$$F_3 = 1 - 1.6 \times 10^{-3}(T_{ref} - T_a)^2, \tag{3.32}$$

where T_{ref} is 298 K in temperate zones. Since the temperature difference is squared, F_3 decreases and r_c increases when the temperature departs from T_{ref}. Note that when $|T_{ref} - T_a| = 25$ K, $F_3 = 0$, indicating that the canopy resistance becomes infinitely large and all transpiration ceases. In practice, F_3 generally is required to be a very small positive number (0.0001).

The final F-factor represents the influence of soil moisture on the canopy resistance. There are several different approaches to this term, but they all attempt to determine the amount of available soil moisture for transpiration. Jacquemin and Noilhan (1990) define

$$F_4 = \frac{\Theta_2 - \Theta_w}{\Theta_{fc} - \Theta_w}, \tag{3.33}$$

where Θ_2 is the volumetric water content of the bulk soil layer in which the majority of the roots are located. Other schemes compute a root-layer average soil moisture (Chen *et al.* 1996; Chen and Dudhia 2001) for which a two-layer rooting zone yields

$$F_4 = \sum_{i=1}^{2} \frac{(\Theta_i - \Theta_w)d_{z_i}}{(\Theta_{fc} - \Theta_w)(d_{z_1} + d_{z_2})}, \tag{3.34}$$

where d_{z_i} is the depth of the ith soil layer. Thus, F_4 decreases and r_c increases as the soil moisture is depleted towards the wilting point when $F_4 = 0$ and transpiration ceases.

A third expression for the transpiration from vegetation is found in Viterbo and Beljaars (1995) in which

$$Q_{EV} = (1 - C_l)\sigma_f \frac{\rho L_v}{r_a + r_c}\left[q_s(T_g) - T_a\right], \tag{3.35}$$

where $r_a = 1/(C_h u)$, C_h is a transfer coefficient, u is the near-surface wind speed, C_l is the interception reservoir fraction for the wet canopy, and

$$r_c = \frac{r_{c\,min}}{LAI} f_1(PAR) f_2(\overline{\Theta}). \tag{3.36}$$

In this expression there are only two environmental factors that influence the canopy resistance, the amount of incoming photosynthetically active radiation (PAR) and the mean soil volumetric water content within the rooting zone. Following Sellers (1985), they define the f_1 adjustment factor as

$$\frac{1}{f_1(PAR)} = 1 - a_1 \log\left(\frac{a_2 + PAR}{a_3 + PAR}\right), \tag{3.37}$$

where the values of a_i are related to the vegetation type. The expression for the f_2-factor is basically the same as for g in the Pan and Mahrt (1987) scheme as shown in (3.25).

Finally, Chen *et al.* (1996) and Chen and Dudhia (2001) use the following expression for transpiration, namely

$$Q_{EV} = \sigma_f E_p B_c \left[1 - \left(\frac{W_c}{S}\right)^n\right], \tag{3.38}$$

where

$$B_c = \frac{1 + \Delta/r_r}{1 - r_c C_h u_a + \Delta/r_r}. \tag{3.39}$$

Here Δ is again related to the change of saturation vapor pressure with respect to temperature as defined by (3.12) by Mahrt and Ek (1984), r_c is the canopy resistance as defined by Noilhan and Planton (1989), including the F_1 through F_4 factors, r_r is a resistance that includes an adjustment factor that depends upon the air temperature and surface pressure and is defined as

$$r_r = \frac{4\sigma T_a^4 R_d}{p c_p C_h u_a} + 1, \tag{3.40}$$

where u_a is the surface layer wind speed and in which the transfer coefficient

$$C_h = \frac{k^2}{R} \frac{G_2}{\ln(z/z_0)\ln(z/z_{0h})}, \tag{3.41}$$

where

$$G_2 = \begin{cases} e^{-aRi}, & \text{stable,} \\ 1 - \dfrac{15Ri}{1 + A}, & \text{unstable.} \end{cases} \tag{3.42}$$

and

$$A = \frac{70.5k^2\sqrt{-Ri(z/z_0)}}{\ln(z/z_0)\ln(z/z_{0h})}. \tag{3.43}$$

in which R (= 1) is the ratio of exchange coefficients, Ri is the Richardson number as defined previously, and a is a constant often assumed to be 1.0. These expressions are from Mahrt (1987) for the stable case, and Holtslag and Beljaars (1989) for the unstable case.

The canopy evapotranspiration from schemes that have separate equations for the ground surface and the vegetation canopy is often calculated directly using the following equation from Sellers *et al.* (1986):

$$Q_{EV} = \frac{[e_s(T_c) - e_a]\rho c_p}{(\bar{r}_c + \bar{r}_b)\gamma} \left(\frac{\sigma_w}{\bar{r}_b} + \frac{1 - \sigma_w}{\bar{r}_b + \bar{r}_c}\right), \tag{3.44}$$

where the overbars refer to resistances that are bulk values. This again is the same basic equation for latent heat flux as seen in Chapter 2, but using canopy temperature T_c and incorporating the reduction in Q_E from the interception of precipitation from leaves and using somewhat different resistance formulations.

The canopy resistance used by Sellers *et al.* (1986) also is different from the previous expressions, and is a rather complicated function that depends upon a large number of factors. The canopy resistance is defined as

$$\frac{1}{r_c} = \sigma_f N_c f_3 f_4 f_5 \int_0^{LAI} \int_0^{\pi/2} \int_0^{2\pi} \frac{O(\xi, \theta)}{r_l(F, \kappa, \xi, \theta)} \sin(\theta)\, d\xi\, d\theta\, dLAI, \tag{3.45}$$

where σ_f is the fractional canopy coverage (0 to 1), N_c is the fraction of LAI that consists of live, photosynthesizing leaves, f_3 is an adjustment factor for water stress, f_4 is an adjustment factor for leaf temperature, f_5 is the adjustment factor for vapor pressure deficit, $O(\xi, \theta)$ is the leaf angle distribution function, where θ is the leaf angle above a horizontal plane and ξ is the leaf azimuth angle, and r_l is the resistance of an individual green leaf, where F is the photosynthetically active radiation incident upon the leaf and κ is the leaf conductivity.

Many other approaches to the calculation of transpiration exist in the literature. In addition to the big-leaf canopy models described above (see also Dai *et al.* 2003), multi-layer canopy models are available that integrate the fluxes from each canopy layer to give the total flux (Wang and Jarvis 1990; Leuning *et al.* 1995). Dai *et al.* (2004) develop a two-big-leaf canopy model that differentiates between sunlit and shaded leaves to overcome problems with the overestimation of transpiration seen in single big-leaf canopy models.

Unfortunately, canopy models that predict canopy or stomatal resistance directly from environmental factors, while neglecting the fundamental underlying mechanisms, have a general problem in that they tend to be specific to a particular vegetation type and must be readjusted for different vegetation types and perhaps even different climate conditions (Collatz *et al.* 1991). Thus, physiological schemes for estimating stomatal resistance have also been developed (Ball *et al.* 1987; Kim and Verma 1991; Collatz *et al.* 1991). Although empirically based, these schemes mimic the physiological response of the vegetation to determine the appropriate regulation between the conflicting roles of permitting CO_2 to diffuse to the leaf to support photosynthesis and restricting the diffusion of water vapor out of the leaf. Dai *et al.* (2004) and Daly *et al.* (2004) develop other examples of canopy models that include consideration of photosynthesis in their formulation. Comparisons between the stomatal resistance calculation of Noilhan and Planton (1989) and those from physiological approaches by Niyogi and Raman (1997) indicate that the

physiological schemes tend to produce a better trend in stomatal resistance, but also have a large amount of variability. Similar results affirming the claim that photosynthesis-based schemes reproduce the measured stomatal resistances more closely are seen in Collatz *et al.* (1991), Baldocchi and Rao (1995), and Su *et al.* (1996). Unfortunately, these more complex physiological models are computationally more expensive than the simple big-leaf canopy models discussed above and require information on photosynthesis rates and CO_2 concentrations at the leaf surface that is not readily available (Niyogi *et al.* 1998). Thus, these more sophisticated and more realistic schemes are not presently used in operational numerical weather prediction models.

3.4.4 Subgrid variability

Some of the land surface models allow for heterogeneous land surfaces within each grid cell of the model domain. This subgrid variability in the surface forcing is represented in the model by dividing the grid cell into a number of homogeneous subregions. The number of subregions depends upon either the number of different vegetation types or soil types, or may be specified in advance. As first discussed by Avissar and Pielke (1989), it is assumed that the horizontal fluxes between the homogeneous land surface patches are small compared to the vertical fluxes and that the atmospheric conditions above the grid cell are the same for each of the subgrid patches. Thus, within each grid cell, the horizontal areas of each type of surface class are summed even if they are not adjacent to each other. This aggregation procedure greatly reduces the total number of subgrid classes needed for the grid cell, since it depends upon the surface class only and not the patch location within the grid cell. The total flux of energy from the surface to the atmosphere within each grid cell is defined as

$$Q_x = \frac{\sum_{i=1}^{n} A_i Q_x}{\sum_{i=1}^{n} A_i}, \tag{3.46}$$

where Q_x is the flux (latent, sensible, ground, longwave radiation, etc.), A_i is the area of the ith surface class, and n is the number of surface classes, or patches, within the grid cell. Avissar and Pielke (1989) suggest that while mesoscale atmospheric patterns can be simulated without including the subgrid variability in land surface conditions, the inclusion of subgrid variability allows for the prediction of the micrometeorological conditions within each land class or patch that may be important to end users of forecast information.

3.5 Momentum transfer

In simple terms, the roughness length z_0 is increased when a ground surface is vegetated. This leads to a rougher surface, such that the vertical mixing is enhanced. Another way of looking at it is to note that as the roughness length increases, the resistance decreases, and thus the surface fluxes of sensible and latent heat are larger.

In land surface schemes that include a single temperature for the combined bare soil and vegetation surface, the roughness lengths typically are defined through information on the dominant vegetation type within the grid cell. These roughness lengths thus already incorporate the gross effects of vegetation on the vertical mixing. However, in land surface schemes that have separate equations for ground and vegetation canopy temperatures, there are several additional roughness lengths that are needed to determine the fluxes. In these schemes, there are typically two different types of vegetation: ground cover and canopy. This requires the addition of one extra resistance and some reconfiguring of the layers over which the resistances are calculated (Sellers *et al.* 1986). With a canopy, the resistances that need to be specified are:

1. resistance from the top of the ground cover and soil surface to the canopy height (r_d);
2. resistance within the canopy layer ($\bar{r}_b$);
3. resistance from the canopy height to within the atmospheric surface layer (r_a) so that the flux calculations can be completed.

The first resistance r_d is defined in Sellers *et al.* (1986) as

$$r_d = \int_0^h \frac{1}{K_m}\, dz = \frac{c_2}{u_c}, \tag{3.47}$$

where K_m is the eddy viscosity ($m^2\,s^{-1}$), h is the height of the canopy, c_2 is a surface-dependent constant, and u_c is the wind speed at the canopy level. For the second resistance $\bar{r}_b$, note that if r_{bi} is assumed to be the resistance of an individual leaf, then $\bar{r}_b$ is the resistance of all the leaves in the canopy. Using various scaling arguments, one can arrive at the resistance of an individual leaf

$$r_{bi} = \frac{c_s}{L_i\sqrt{u_i}}, \tag{3.48}$$

where c_s is another transfer coefficient, L_i is the leaf area (m^2), and u_i is the wind speed on the individual leaf i. This can then be summed over all leaves to obtain

$$\frac{1}{\bar{r}_b} = \sum_{i=1}^{n} \frac{L_i \sqrt{u_i}}{c_s P_s}. \tag{3.49}$$

where P_s is a shelter factor defined as the ratio of the observed transfer coefficient within the canopy to the transfer coefficient of an individual leaf in isolation (Monteith and Unsworth 1990). If one further assumes that the leaf density is constant within the canopy, then

$$\frac{1}{\bar{r}_b} = \int_{z_{c\,bottom}}^{z_{c\,top}} \frac{LAI\sqrt{u}}{c_s P_s}\, dz = \frac{c_1}{\sqrt{u_c}}. \tag{3.50}$$

Finally, the last resistance that needs to be calculated is the resistance from the canopy height to within the atmospheric surface layer. This is our old friend

$$r_a = \frac{1}{k u_*}\left[\ln\left(\frac{\bar{z}_{eff}}{h}\right) - \psi_h\left(\frac{\bar{z}_{eff}}{L}\right)\right]. \tag{3.51}$$

Note that the resistances r_d and $\bar{r}_b$ are both defined using coefficients (c_1 and c_2) that are dependent upon the vegetation type. Thus, these schemes have yet more parameters that are dependent upon the vegetation type as specified in the database used by the numerical model, which typically only incorporates 15–30 vegetation types compared to the hundreds that are estimated from satellite data.

3.6 Soil moisture availability

It is obvious that when over a certain time period the evapotranspiration is greater than the rainfall over the same time period, then the difference represents the amount of water that must be supplied from the soil or some other source. The complicating factors in trying to calculate this water transport are that plants have developed strategies for growth and reproduction that maximize the odds of survival of their species, and that water–soil interactions may not be as simple as originally hoped. Canny (1998) suggests that managing the stream of water that plants need to survive "dominates the life process of plants." Accordingly, a lot of new terminology (at least to meteorologists) must be introduced before one can understand how models of soil and vegetation operate.

We begin with a few new terms from soil science and botany. Potential (short for potential energy) is one of the most important new terms. The basic idea is that since work is performed by water as it moves from one system to

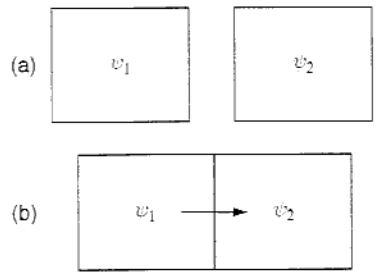

Figure 3.10. Two equilibrium soil water systems that (a) are not interacting and (b) that are interacting after coming in contact with each other. Water flows from high potential to low potential, with $\psi_1 > \psi_2$.

another, then water in an equilibrium system has the potential to do work, and hence the energy is called potential energy. This terminology replaces terms such as suction, tension, stress, head, and pressure that were used previously in soil sciences. Potential as used in meteorology generally has units of $J\,kg^{-1}$ or meters and is noted by the Greek letter ψ. Potential can be thought of as the partial specific Gibbs free energy of the water in the system. To convert potential from units of $J\,kg^{-1}$ to m, note that multiplying or dividing by gravitational acceleration g does the trick. To convert potential from units of $J\,kg^{-1}$ to bars, divide by 100.

As an example, examine two soil water systems ψ_1 and ψ_2 that are presently in equilibrium (Fig. 3.10), have different potentials with $\psi_1 > \psi_2$, and are initially separate from each other. When these two systems are brought into contact with each other, then water flows from system 1 into system 2 as water is defined to flow from higher potential to lower potential, since work must be done to move the water. Thus, the water flux density (F_w) with units of $kg\,m^{-2}\,s^{-1}$ is related to the gradients of potential, such that

$$F_w = -k_w \frac{\partial \psi}{\partial x}, \tag{3.52}$$

where k_w is the hydraulic conductivity. This basic relationship is called Darcy's law (see Houser 2003). Typically, for soils and plants it is assumed that the water flux density, F_w, is only influenced by vertical gradients in potential, although horizontal gradients are possible owing to horizontal variations in rainfall or being close to streams, lakes, or rivers.

Potential is produced by a number of different physical mechanisms, depending in part upon whether one is studying the potential for plants or for soils. One of these mechanisms is directly related to the pressure potential (ψ_p) that results from an overall pressure that is different from the reference

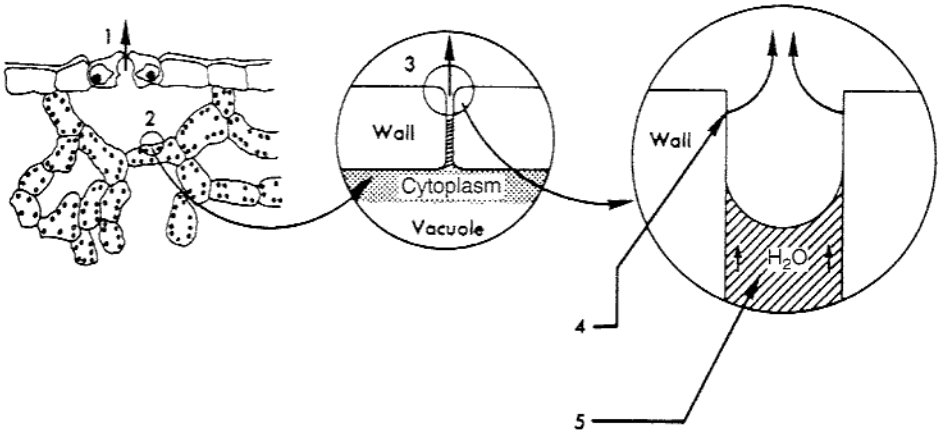

Figure 3.11. Illustration of the rise of sap within a tree as a result of transpiration. (1) Transpiration through the stomates (indicated by heavy upwardly directed arrows), (2) evaporation from microcapillaries into the intercellular space of the stomates, (3) partial drying of the microcapillary cell walls, (4) water from film attracted by surface tension, and (5) rising of whole water column because of cohesive force of water. From Levitt (1974), used with permission from Elsevier.

pressure (i.e., atmospheric pressure). If $p > p_{ref}$, then $\psi_p > 0$. For plants, pressure potential is due to the effects of surface tension (capillarity), since the water system in most plants is unbroken from roots to leaves. As described in Levitt (1974), the microcapillaries that supply water to stomates within the leaves are very thin, of the order of 0.1 μm. As the stomates open to obtain carbon dioxide from the atmosphere, transpiration occurs and to replace the water vapor in the intercellular space within the stomates, evaporation of water occurs within the microcapillaries (Fig. 3.11). As the microcapillary water evaporates, the walls of the microcapillaries partially dry and the force of adhesion between the walls of the microcapillaries and water pulls the water towards the stomates. The column of water between the stomates and the roots then moves en masse owing to the force of cohesion between the water molecules. This process is called the cohesion theory for water movement within plants. Calculations indicate that this process could supply water to trees that reach 300 m in height, much higher than any trees observed today. While there are some who contest the cohesion theory for water movement in plants, it remains the most widely accepted theory in explaining plant water movement (Taiz and Zieger 2002). Canny (1998) provides a summary of the difficulties and challenges in trying to understand water movement in plants and offers an alternative to cohesion theory. For soils, $\psi_p = 0$ unless the soil is

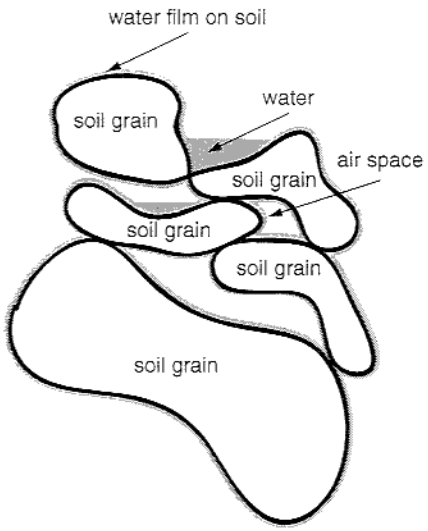

Figure 3.12. Soil grains surrounded by a thin layer of water (gray shading), due to adsorptive effects of the soil, and also supporting small areas in which water can collect.

supersaturated and for this case $\psi_p > 0$. The pressure potential is never less than zero for soils.

A different mechanism for soils is directly related to the matric potential (ψ_m). Matric potential is the portion of potential that results from the colloidal matrix, or the intercellular substance of a tissue or mass, of the soil system. Thus, matric potential includes the effects of adsorption (the gathering of water in a condensed layer on a surface), capillarity, and curved air–water interfaces. It is found that soil particulates adsorb water such that a very thin layer of water surrounds each soil grain (Fig. 3.12). This water layer may not be very thick, but it is very important to the overall moisture level in the soil. Adsorptive forces are very strong and it is difficult to remove water from the soil when the water layer is reduced to four or five molecules in thickness. If soils are examined very closely, then both air spaces in between the soil grains and wedges in which water can collect are observed. Thus, soil is highly fractal in structure.

The third type of potential is osmotic potential (ψ_o), produced by the combined effects of all solute species present in the soil or plant water system. In plants, the osmotic potential is the potential difference between water in solution and pure free water. It is defined as

$$\psi_o \cong -cRT, \tag{3.53}$$

where c is the moles of solute per unit weight of the mixture (mol kg^{-1}), R is the universal gas constant of 8.31 J K^{-1} mol^{-1}, and T is the temperature in kelvin. This expression is called the van't Hoff relation (Taiz and Zieger 2002). It is found that ψ_o is either zero or negative. In soils, osmotic potential happens mainly when salts are present in the soil; otherwise the osmotic potential is zero. For plants, the sum of the pressure potential and the osmotic potential is called the mesophyll potential ($\psi_m = \psi_o + \psi_p$) and represents the total attraction of the intercellular tissues for water.

The final potential that needs to be defined is the gravitational potential (ψ_g), which is that portion of the potential attributable to the gravitational force field and is dependent upon the vertical elevation of the water. Thus,

$$\psi_g = \rho_w g(z - z_{ref}), \tag{3.54}$$

where ρ_w is the density of water, g is the acceleration due to gravity, z is the height of the water system, and z_{ref} is the reference height to which it is being compared (typically the height of the ground surface). The total potential for plants and soil can then be defined as

$$\psi_{plant} = \psi_{m_{plant}} + \psi_g = \psi_{p_{plant}} + \psi_{o_{plant}} + \psi_g, \tag{3.55}$$

$$\psi_{soil} = \psi_{m_{soil}} + \psi_g. \tag{3.56}$$

Now that potential has been defined, it is important to understand how potential is observed and what it means physically. Both perhaps can be explained by examining one method for calculating potential. While potential can be observed using tensiometers, gas pressure devices can also be used (Marshall *et al.* 1996). The most important component of a gas pressure device is a horizontal porous ceramic plate that allows water to pass through the plate while also impeding the flow of air. Below the ceramic plate in these devices is a water reservoir at atmospheric pressure that is in direct contact with the plate. Placed on top of the ceramic plate are soil samples. And surrounding everything is a chamber into which gas can be pumped and measured (Fig. 3.13). If the air in the chamber is at atmospheric pressure, then water flows into the soil if the soil is initially dry owing to the soil matric potential – the adsorptive effects of the soil. At point A in Fig. 3.13, $\psi_p = 0$ since the soil is at the reference pressure and the soil is not saturated. However, $\psi_m < 0$ at this same point owing to the adsorptive effects of the soil matrix and the soil not being saturated, and thus water moves upward into the soil. The value of ψ_m for the soil can be determined by increasing the air pressure in the container until no water flows, yielding

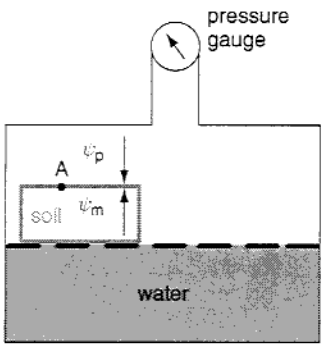

Figure 3.13. Schematic of a gas pressure device used to measure pressure and thereby matric potential. Water fills the bottom portion of the container, with a ceramic plate porous to water but not to air separating the water from the soil (dashed line). Initially, water flows into the unsaturated soil owing to the adsorptive effects of the dry soil or its matric potential. By increasing the pressure in the chamber, this upward water movement can be stopped. At this time, the pressure and matric potentials are equal.

$$\psi_{m_{soil}} = \psi_p = \frac{(p_{ref} - p)}{\rho_w} < 0. \tag{3.57}$$

As indicated by (3.57), the values of both soil and plant potential typically are negative.

Observations indicate that transpiration removes a considerable amount of water from the plant tissues as the stomates expose the water in the plant to evaporation. The rate of transpiration thus determines the rate at which the soil must supply water to the plant. For some woody plants, the plant potential decreases rapidly as transpiration increases even when the water supply to the roots is adequate (Camacho-B *et al.* 1974). In contrast, for herbaceous plants studied under identical conditions, the plant potential remains nearly constant across a fairly large range of transpiration rates. Thus, it appears that plants can be grouped into three broad categories based upon their response to environmental conditions: (1) plants with inefficient water transport systems and strong stomatal control to regulate water loss, (2) plants with both efficient water transport systems and strong stomatal control, and (3) plants with very efficient water transport systems and little stomatal control (Camacho-B *et al.* 1974). The different responses of these three broad plant categories can be generalized as being due to differences in resistance of the soil–plant system at the leaf–air interface (stomatal control) and at the root–soil interface (water transport). Therefore, what happens at these soil–plant–air interfaces can be important in defining the rate of transpiration.

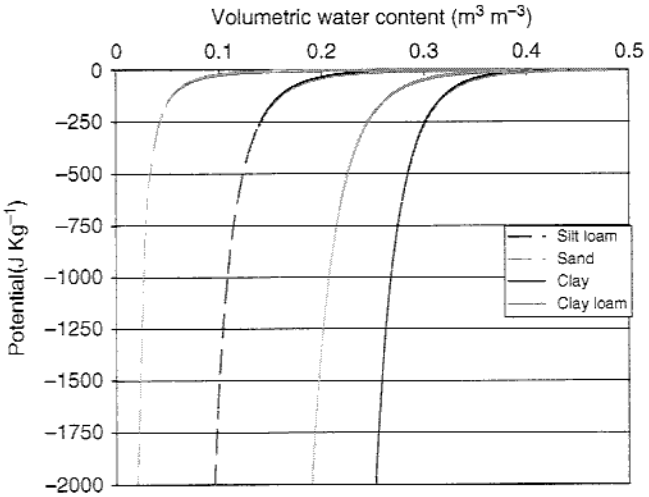

Figure 3.14. Characteristic curves of soil potential (J kg^{-1}) versus volumetric water content for four different types of soils: sand, silt loam, clay loam, and clay. Data based upon coefficients from Cosby *et al.* (1984).

The root–soil interface resistance is greatly influenced by the soil potential, which is a function of the soil water content. Observations indicate that as the volumetric water content of the soil decreases from saturated conditions (values of ~0.4–0.5), the soil potential at first decreases very little. However, eventually a point is reached at which the soil potential quickly becomes more negative as the volumetric water content decreases slightly owing to the adsorptive effects of the soils for water (Fig. 3.14). Enough similarity is seen within soils that characteristic curves have been identified for various soil types that relate the soil potential to the water content of the soil. Expressions that define these curves are used within the soil–vegetation–atmosphere transfer models.

The evolution of the plant and soil potentials in relation to each other over a sequence of days indicates that each morning after the sun rises, the plant potential is lowered in order for water to flow into the plant through the root system (Fig. 3.15). The plant potential reaches a minimum sometime typically in the afternoon, and then increases toward nighttime as the demand for water decreases. During this time period, enough water has been removed from the initially near saturated soil that a noticeable difference is seen, but it is not very large. During the night, the plant and soil potentials equilibrate, as the plant no longer has any need to move water. As day two dawns, the plant again reduces the potential and the uptake of water from the soil begins again. This process continues over several days, and perhaps even weeks, depending upon the water needs of the plant and the atmospheric conditions, until at some time (assuming no new rain has fallen), the plant potential has to decrease to very

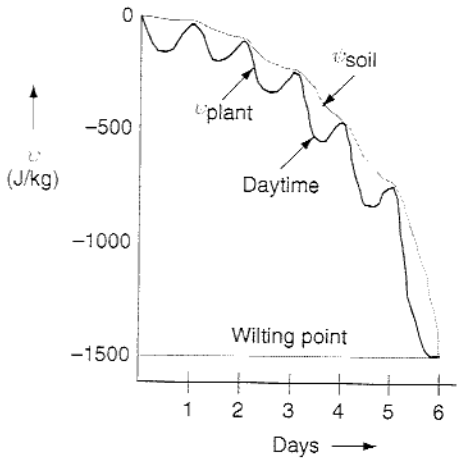

Figure 3.15. Evolution of plant potential and soil potential over a multiple day period in which no rainfall reaches the ground surface. As the sun rises, the plant potential decreases in order to move water from the soil to the plant system. The potential difference is related to the amount of water flowing into the plant. At night, the plant and soil potentials are equal as no water is flowing in the plant–soil system. After several days, the soil potential drops so low (owing to water loss due to the plant) that the plant can no longer draw more water from the soil. This is the wilting point, and indicates that transpiration has ceased.

negative values in order to continue to move water from the soil to the plant. Eventually, the plant reaches its wilting point, when capillary water becomes unavailable to the plant cells and the plant wilts. Thus, once the soil potential is equal to or less than the plant potential at the wilting point, water flow to the plant stops and transpiration ceases. The potential value at the wilting point for most plants is close to $-1500\,\mathrm{J\,kg^{-1}}$, although potentials as low as $-4000\,\mathrm{J\,kg^{-1}}$ have been observed for plants in semi-arid regions (Peláez and Bóo 1987).

To model the behavior of plants and soils and their interactions, the same resistance approach developed earlier for the calculations of the fluxes of sensible and latent heat is used. However, the potential difference for plant and soil interactions is the difference in potential of the plant and soil systems. So one needs to be able to determine the plant and soil potentials, and the required resistances, in order to calculate the water flux into the plant and evapotranspiration. Many soil–vegetation–atmosphere parameterizations avoid calculating the plant potential, assuming that the plant water needs are met as long as the soil potential is above the wilting point.

The characteristic curves of soil potential versus water content of the soil provide the empirical results necessary to model this type of behavior

(Fig. 3.14). As seen previously, the soil potential remains fairly steady as the volumetric water content is first decreased from its value at saturation, but then a point is reached where the soil potential undergoes a rapid decrease as the volumetric water content is decreased slowly. As might be imagined, the point at which the soil potential begins to decrease rapidly is important to the behavior of the soil–plant system. The characteristic curves can be fitted for the various soil texture types, yielding an expression that relates the soil potential to the volumetric water content

$$\psi_{soil} = \psi_s \left(\frac{\Theta}{\Theta_s} \right)^{-b}. \tag{3.58}$$

where ψ_s is the saturation matric potential ($\psi_s < 0$), b is an empirically determined constant, and Θ_s is the soil porosity. Porosity represents the maximum amount of water that the soil can hold, assuming all the pores that contribute to a change in water storage are filled with water. It also is referred to as the volumetric water content at saturation. The parameters ψ_s, Θ_s, and b depend upon the soil texture class. For example, sand has $b \sim 4$, $\psi_s \sim -0.12\,\mathrm{J\,kg^{-1}}$, and $\Theta_s \sim 0.39$. In contrast, clay has $b \sim 11$, $\psi_s \sim -0.41\,\mathrm{J\,kg^{-1}}$, and $\Theta_s \sim 0.48$.

The shapes of the characteristic curves are very sensitive to the values of b (Fig. 3.16). According to Cosby *et al.* (1984), who examined 1448 different soil samples, the standard deviations in the values of b for the 11 soil types vary

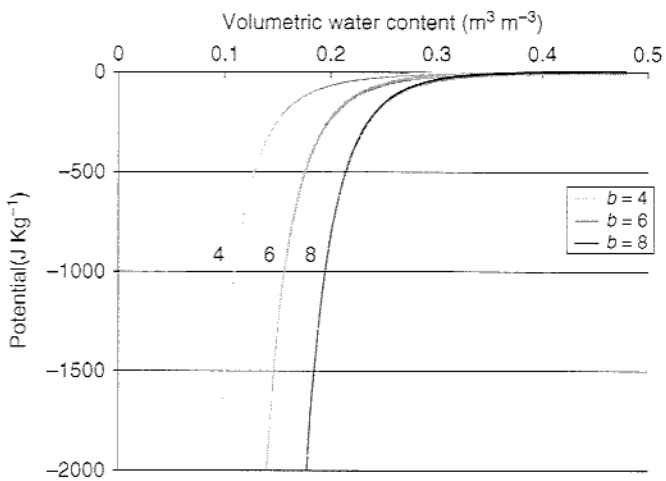

Figure 3.16. Characteristic curves of soil potential ($\mathrm{J\,kg^{-1}}$) versus volumetric water content ($\mathrm{m^3\,m^{-3}}$) for a soil using three different values for the b parameter and with all other parameters constant. Here it is assumed that $\psi_s = -1\,\mathrm{J\,kg^{-1}}$ and $\Theta_s = 0.50$.

from a minimum of 1.38 for sand to a maximum of 4.33 for silty clay loam. This uncertainty in the values of b results in a fairly large uncertainty in the values of soil potential. The values in Cosby *et al.* (1984) show that the variations of b within the soil classes are as large as the differences in b between soil classes. For values of volumetric water content near saturation, this uncertainty in the value of b makes little difference in the curves (Fig. 3.16). However, as the volumetric water content decreases, this uncertainty can lead to differences in potential of more than $500\,\mathrm{J\,kg^{-1}}$ for moderate values of volumetric water content (0.2–$0.3\,\mathrm{m^3\,m^{-3}}$) and differences of more than $1000\,\mathrm{J\,kg^{-1}}$ for smaller values of volumetric water content ($\Theta < 0.2\,\mathrm{m^3\,m^{-3}}$). This can have a significant difference on determining when the wilting point is reached and transpiration ceases, potentially resulting in large errors in evapotranspiration when the value of soil potential approaches the wilting point.

The classification of the soil texture is important as it is used to define the various parameters that relate to soil–water interactions. First, the water holding properties differ between the various soil textures, leading to significantly different values of the volumetric water content at the porosity, field capacity, and wilting point (Fig. 3.17). Second, the values of b and ψ_s also depend upon soil texture and vary across the soil texture triangle. While the values of ψ_s vary across a relatively small range, the values of b vary from 2.79 for sand to 11.55 for light clay (Table 3.1). Since b is the exponent in (3.58) in which the soil potential is related to the volumetric water content, it plays a large role in determining the soil potential. The standard deviations of b found by

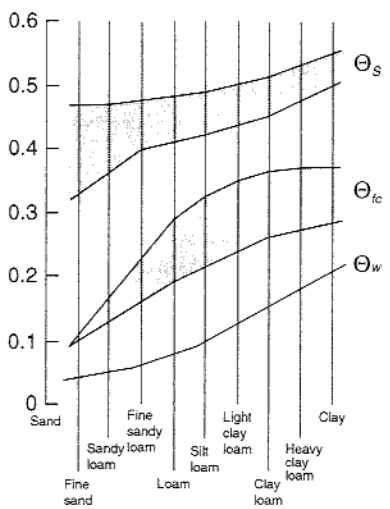

Figure 3.17. Water holding properties of various soils. Shading highlights the variation in the parameters for a given soil type. After Houser (2003).

Table 3.1. *Mean and standard deviations of the b parameter for each of 11 soil classes and the number of samples tested. From Cosby* et al. *(1984).*

Soil class	No. samples	Mean value of b	Standard deviation
Sandy loam	124	4.74	1.40
Sand	14	2.79	1.38
Loamy sand	30	4.26	1.95
Loam	103	5.25	1.66
Silty loam	394	5.33	1.72
Sandy clay loam	104	6.77	3.39
Clay loam	147	8.17	3.74
Silty clay loam	325	8.72	4.33
Sandy clay	16	10.73	1.54
Silty clay	43	10.39	4.27
Light clay	148	11.55	3.93

examining a large number of soil samples (Clapp and Hornberger 1978; Cosby *et al.* 1984) indicate a fair amount of uncertainty in the exact soil potential at a given location for any predicted or measured volumetric water content.

Recall that soil texture typically is defined from worldwide soil surveys (see Fig. 3.8) that vary in quality and degree of detail from country to country. Once the soil texture is known at a given grid point, the results of Cosby *et al.* (1984) can be used to specify soil porosity, saturated matric potential, saturated hydraulic conductivity, and the exponential parameter b. However, the volumetric water content field capacity and wilting point are not provided by Cosby *et al.* (1984) and so must be computed. Generally, the field capacity is determined either as a fraction of the porosity (75% of porosity as in Noilhan and Planton 1989) or by determining the soil moisture value that yields a hydraulic conductivity equal to a specific drainage flux. For example, Wetzel and Chang (1987) define field capacity as the volumetric soil water content that produces a value of hydraulic conductivity of $0.1\,\mathrm{mm\,day^{-1}}$, whereas Chen and Dudhia (2001) use $0.5\,\mathrm{mm\,day^{-1}}$. The wilting point typically is determined using a constant value of soil potential below which plants have extreme difficulty in extracting water from the soil, and then calculating the volumetric soil water content for that value of potential. As mentioned previously, a potential value of between -1500 and $-2000\,\mathrm{J\,kg^{-1}}$ is often used for the wilting point.

Once the soil potential is calculated, the next step is to determine the water transport. The soil hydraulic conductivity κ_{soil}, which is inversely related to the soil resistance, can be specified as (Campbell 1974)

$$\kappa_{soil} = \kappa_s \left(\frac{\Theta}{\Theta_s}\right)^{2b+3} = \frac{\alpha_f}{r_{soil}} = \kappa_s \left(\frac{\psi_s}{\psi_r}\right)^{(2B+3)/B}, \tag{3.59}$$

where κ_s is the value at saturation, b and B are specified constants that depend upon soil type (the b parameter is the same as used in determining soil potential), ψ_r is the soil potential in the root zone, and α_f is a conversion factor. Values of κ_s vary from 10^{-4} to 10^{-5} m s^{-1} for sand to 10^{-6} to 10^{-9} m s^{-1} for clay. Larger values of b produce smaller values of conductivity and larger values of soil resistance as Θ decreases.

When thinking about soil moisture availability, it is important to define all the sources and sinks of moisture. The uptake of water by plants is a sink for soil moisture, whereas precipitation provides a source for soil moisture. Finally, given a little thought one could probably realize that soil moisture can flow between different soil layers and perhaps even drain away. This drainage term could be either a source or a sink, depending upon the direction of movement of the water in the soil.

One way to determine changes to the soil volumetric water content Θ is to use Darcy's law, which relates the change in potential to the flow rate, such that

$$\frac{\partial \Theta}{\partial t} = \frac{\partial}{\partial z}\left[\left(\frac{\kappa_{soil}}{\rho_w g}\right)\frac{\partial \psi}{\partial z}\right] = \frac{\partial}{\partial z}\left(\frac{\kappa_{soil}}{\rho_w g}\frac{\partial \psi}{\partial \Theta}\frac{\partial \Theta}{\partial z}\right), \tag{3.60}$$

where κ_{soil} is the hydraulic soil conductivity (m s^{-1}) as defined earlier. Recalling the discussion of soil potential, there exist empirical relationships for the characteristic curves of soil matric potential and also a relationship describing the hydraulic soil conductivity. Thus, substituting (3.58) and (3.59) into an equation describing Darcy's law yields

$$\begin{aligned}\frac{\partial \Theta}{\partial t_{matric}} &= \frac{\partial}{\partial z}\left[\frac{\kappa_s}{\rho_w g}\left(\frac{\Theta}{\Theta_s}\right)^{2b+3}\left(\frac{-b\psi_s}{\Theta_s}\right)\left(\frac{\Theta}{\Theta_s}\right)^{-(b+1)}\frac{\partial \Theta}{\partial z}\right] \\ &= \frac{\partial}{\partial z}\left[\frac{-\kappa_s b \psi_s}{\rho_w g \Theta_s}\left(\frac{\Theta}{\Theta_s}\right)^{b+2}\frac{\partial \Theta}{\partial z}\right].\end{aligned} \tag{3.61}$$

The result is that water diffuses towards lower values of water content, which is just what one would expect.

We also need to develop a similar equation for the gravitational potential using Darcy's law. Recall that

$$\psi_g = \rho_w g(z - z_{ref}). \tag{3.62}$$

If this expression is plugged into the potential in Darcy's law, then

$$\frac{\partial \Theta}{\partial t_{grav}} = \frac{\partial}{\partial z}\left(\frac{\kappa_{soil}}{\rho_w g}\frac{\partial \psi_g}{\partial z}\right) = \frac{\partial}{\partial z}\left(\frac{\kappa_{soil}}{\rho_w g}\rho_w g \frac{\partial z}{\partial z}\right) = \frac{\partial}{\partial z}(\kappa_{soil}). \tag{3.63}$$

Again, using knowledge of the equation for the hydraulic soil conductivity, one finds that

$$\frac{\partial \Theta}{\partial t_{grav}} = \frac{\partial}{\partial z}\left[\kappa_s\left(\frac{\Theta}{\Theta_s}\right)^{2b-3}\right] = \frac{\partial}{\partial \Theta}\frac{\partial \Theta}{\partial z}\left[\kappa_s\left(\frac{\Theta}{\Theta_s}\right)^{2b-3}\right]$$
$$= \frac{\kappa_s}{\Theta}\left(\frac{\Theta}{\Theta_s}\right)^{2b-2}(2b+3)\frac{\partial \Theta}{\partial z}. \tag{3.64}$$

These two equations, (3.61) and (3.64), determine the flow between layers and the drainage, while uptake by plants is calculated using the plant transpiration rate (i.e., the latent heat flux) and the precipitation rate is calculated using the atmospheric model. Plant uptake typically occurs over specified soil layers. For example, most vegetation schemes assume that the lowest soil layer is below the plant rooting depth (Fig. 3.18). Water is removed from the soil layers in proportion to their depth and the available water in each layer.

The expressions for the time rate of change in the volumetric water content for a three-layer soil model are fairly consistent in the literature and are based upon Richards' equation that extends Darcy's law to non-saturated soil conditions. Chen *et al.* (1996) and Chen and Dudhia (2001) predict the volumetric water content for four soil layers using

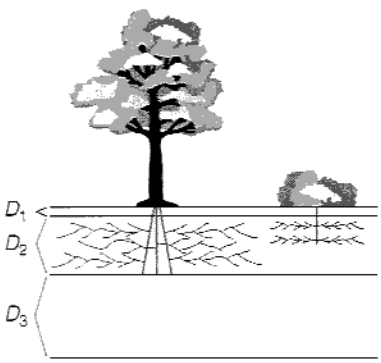

Figure 3.18. Illustration of depth over which roots are assumed to exist and can remove water from the soil. Vertical soil layers are labelled D_1, D_2, and D_3. Trees (or shrubs) and ground cover may have different rooting depths. After Sellers *et al.* (1986).

$$dz_1 \frac{\partial \Theta_1}{\partial t} = -D\left(\frac{\partial \Theta}{\partial z}\right)_{z_1} - \kappa_{z_1} + P_d - R - \left[\frac{(Q_{EB} + Q_{EV_1})}{L_v \rho_w}\right], \tag{3.65}$$

$$dz_2 \frac{\partial \Theta_2}{\partial t} = D\left(\frac{\partial \Theta}{\partial z}\right)_{z_1} - D\left(\frac{\partial \Theta}{\partial z}\right)_{z_2} + \kappa_{z_1} - \kappa_{z_2} - \frac{Q_{EV_2}}{L_v \rho_w}, \tag{3.66}$$

$$dz_3 \frac{\partial \Theta_3}{\partial t} = D\left(\frac{\partial \Theta}{\partial z}\right)_{z_2} - D\left(\frac{\partial \Theta}{\partial z}\right)_{z_3} + \kappa_{z_2} - \kappa_{z_3} - \frac{Q_{EV_3}}{L_v \rho_w}, \tag{3.67}$$

$$dz_4 \frac{\partial \Theta_4}{\partial t} = D\left(\frac{\partial \Theta}{\partial z}\right)_{z_3} + \kappa_{z_3} - \kappa_{z_4}, \tag{3.68}$$

where dz is the soil layer depth, D is the soil water diffusivity, κ is the soil hydraulic conductivity, P_d is the precipitation not intercepted by the canopy, R is the surface runoff, and the diffusivity is defined as

$$D = \frac{\kappa(\Theta)}{g} \frac{\partial \psi}{\partial \Theta}, \tag{3.69}$$

where potential has units of J kg^{-1}. As discussed by Chen and Dudhia (2001), this diffusive form of Richards' equation (Richards 1931) is derived under the assumption of a rigid, isotropic, homogeneous, and one-dimensional vertical flow domain (Hanks and Ashcroft 1986). Other forms of the equations governing soil moisture are possible (e.g., Sellers *et al.* 1986).

The calculation of runoff (R) is challenging as it depends upon the vegetation cover, the surface slope, and the soil conditions, which can vary greatly over small distances, yet need to be represented in models that have grid cells representing larger areas. As discussed by Schaake *et al.* (1996), complex runoff models have been developed for large river basins but are not appropriate for use in atmospheric models. Thus, Schaake *et al.* (1996) develop a simple water balance (SWB) model to determine runoff for atmospheric models. The SWB is a two-layer model, where the top layer is a thin layer representing the vegetation canopy and the soil surface and the bottom layer is a thicker layer representing the vegetation root zone in the soil plus the groundwater system. Simple and computationally affordable equations to govern changes in water storage are derived. Surface runoff is defined as

$$R = P_d - I_{max}, \tag{3.70}$$

where I_{max} is the maximum infiltration into the soil. Chen and Dudhia (2001) show how the infiltration is calculated in connection to a four-layer soil model, defining

$$I_{max} = \frac{P_d D_x \left[1 - \exp\left(-\kappa_{dt}\delta_i\left(\kappa_s/\kappa_{ref}\right)\right)\right]}{P_d + D_x\left[1 - \exp\left(-\kappa_{dt}\delta_i\left(\kappa_s/\kappa_{ref}\right)\right)\right]}, \tag{3.71}$$

where D_x is the soil moisture storage deficit specified as

$$D_x = \sum_{i=1}^{4} \Delta z_i(\Theta_S - \Theta_i), \tag{3.72}$$

and where δ_i is the model time in days, $\kappa_{dt} = 3.0$, κ_s is the saturated hydraulic conductivity, which depends upon soil texture, and κ_{ref} is the reference value of hydraulic conductivity ($2 \times 10^{-6}\,\mathrm{m\,s^{-1}}$ in Chen and Dudhia 2001). As discussed in Chen and Dudhia (2001), further effort is needed to calibrate these parameters for various basins across the world. In addition, if runoff occurs at one grid cell then it is possible that the runoff flows into a neighboring grid cell where it infiltrates into the soil, but this effect is not yet taken into account in these simple schemes.

When the soil becomes frozen, then the soil can become even less permeable than unfrozen soil, resulting in significant amounts of runoff. This is because ice in the soil can create nearly impermeable soil layers. Observations suggest that the area of these impermeable layers increases as the ice content of the soil increases (Koren *et al.* 1999). To account for this effect, Koren *et al.* (1999) assume that all precipitation runs off when it falls on these impermeable soil areas and develop an equation to determine the fraction of the model grid cell that contains these impermeable ice layers.

The methodology of most of the vegetation schemes generally is to first calculate the potentials and resistances, then to calculate the evapotranspiration rates and update the values of volumetric water content. But note that the soil potential depends upon the volumetric water content, which is changed by the evapotranspiration, and the evapotranspiration depends upon the ground or canopy temperature, which both depend upon the sensible heat flux. It is clear that there are feedbacks everywhere!

3.7 Radiation

The amount of vegetation above the ground surface influences the amount of radiation received at the ground and available for warming the soil, in addition to the reflective properties of the vegetation that influence the surface albedo.

While radiation is covered in greater depth in Chapters 8 and 9, a few brief points are discussed here. First, many schemes use a single temperature for the soil/vegetation surface. This approach appears to yield good results (Chen *et al.* 1997), even though the difference in temperature between the soil and plants can exceed 5 °C (Mahrt and Ek 1984). Since soil and vegetation temperatures are represented by a single temperature value on a single surface, there are no major changes needed in the model radiation scheme to account for vegetation. However, other schemes include separate temperature equations for the ground, defined as a mixture of bare soil and groundcover vegetation, and the vegetation canopy. These most complex vegetation parameterizations require some modifications to the way in which radiation is handled at the surface vegetation–atmosphere interface.

One approach computes the effects of vegetation on the five radiation components separately (Sellers *et al.* 1986). Thus, there are modifications to the radiation calculations to produce values for direct photosynthetically active radiation (PAR), diffuse PAR, direct near-infrared (NIR), diffuse NIR, and diffuse infrared radiation. These calculations incorporate the multiple reflections of light by the leaves in the canopy and the ground surface (whether vegetated or bare). The albedo is allowed to vary during the daytime, requiring information on leaf angle, and leaf transmission and reflection of radiation. Further information may be found in Dickinson (1983) and Sellers (1985).

One important parameter that is needed to account for the effects of vegetation canopies within the radiation calculations is *LAI*. Assuming that the radiative flux at the top of the canopy is

$$Q_S = S(1 - a)\cos(\zeta)\tau_s = Q_{S_o}, \tag{3.73}$$

then the total energy swept out by the vegetation in the vertical interval dz is

$$dQ_S = Q_{S_o}\sigma_p \, dLAI, \tag{3.74}$$

where σ_p is an attenuation coefficient, or optical depth, that is related to the shape factor of the plant leaves, and $dLAI$ is the vertical increment of *LAI*. Therefore, one can calculate the radiation that reaches the surface through the canopy, yielding

$$Q_{S_{sfc}} = Q_{S_o} e^{-\sigma_p LAI_{max}}. \tag{3.75}$$

This relationship applies to both direct solar radiation flux and diffuse solar radiation flux. For example, if $\sigma_p = 0.4$ and $LAI_{max} = 5$, then we find $Q_{S_{sfc}} = 0.14\ Q_{S_o}$ at the ground surface, indicating that the canopy has greatly reduced the incoming radiation.

3.8 Specifying soil temperature and soil moisture

Now that the soil texture, vegetation class, and vegetation health (σ_f and LAI) have been defined at each grid point, and assuming that sufficient information to define the atmospheric state above the ground surface and the ocean state is available, the remaining parameters needed are soil temperature and soil moisture. Unfortunately, routine observations of soil temperature and soil moisture are not commonly available. Satellites may provide observations of skin temperature, but not for soil temperatures as a function of soil depth. This creates a significant challenge for the initialization of land surface models. The most common approach to overcoming this challenge is the development and use of land data assimilation systems (LDAS).

The general idea behind an LDAS is to force a land surface model with observations in order to constrain the behavior of the land surface model so that the soil temperature and moisture values predicted by the model are reasonable. Mitchell *et al.* (2004) discuss the North American LDAS and Rodell *et al.* (2004) discuss a global LDAS (GLDAS). These projects are very important in providing much improved data for initializing land surface models, and they typically involve a number of institutions owing to the wide variety of expertise needed. Typical forcing fields that are provided to the land surface model are routine hourly surface observations (2 m temperature and specific humidity, 10 m winds, and surface pressure), precipitation (gauge, radar-estimated, satellite-estimated, or model produced), model or satellite-estimated incoming solar radiation and incoming longwave radiation. In general, the observation-based fields are used wherever possible, with the model fields used when the observations are not available. Some LDAS also use model estimates of the relative contributions of convective versus total precipitation. These systems are run both retrospectively and in real time to provide the best analyses to use for selected observational periods of the past and for operational numerical weather prediction.

3.9 Discussion

We have explored how the incorporation of vegetation changes the land surface parameterizations and the additional data sets that are needed to initialize the many soil and vegetation parameters. After all this additional complexity has been added to create a soil–vegetation–atmosphere transfer scheme (SVATS), an important question is how well these schemes reproduce the observed fluxes from the land surface to the atmosphere. Unfortunately, direct measurements of surface fluxes are few, so we instead rely on comparisons to

other variables that are measured. A number of important studies have addressed this question in various ways, and several of these are examined to briefly survey the state of the science.

Comparisons between total water storage, defined as the mean soil moisture multiplied by the soil layer depth, from four different land surface parameterizations and observations are made by Schaake *et al.* (2004). The land surface parameterizations evaluated are the Noah (Chen *et al.* 1996), Mosaic (Koster and Suarez 1996), variable infiltration capacity (VIC; Liang *et al.* 1994), and Sacramento (SAC; Burnash *et al.* 1973) schemes. The schemes are forced using the North American LDAS data over a 3 year period, with the first year of forcing data being used to spin-up the schemes. The values of total water storage are averaged over 17 locations in Illinois where soil moisture observations are made bimonthly. Results from the final 2 year period (1997–1999) indicate a strong correlation between the simulated and observed values of total water storage (Fig. 3.19). In general, the simulated total water storage values from the Noah and SAC schemes agree well with the observations, although there is a fair amount of scatter in the data points. The Mosaic and VIC schemes do not compare well with the observations, both underestimating the total water storage. These results suggest that land surface schemes may be able to simulate mean soil moisture values over relatively large geographic areas, but it is not clear how well these schemes can do at providing accurate point measurements

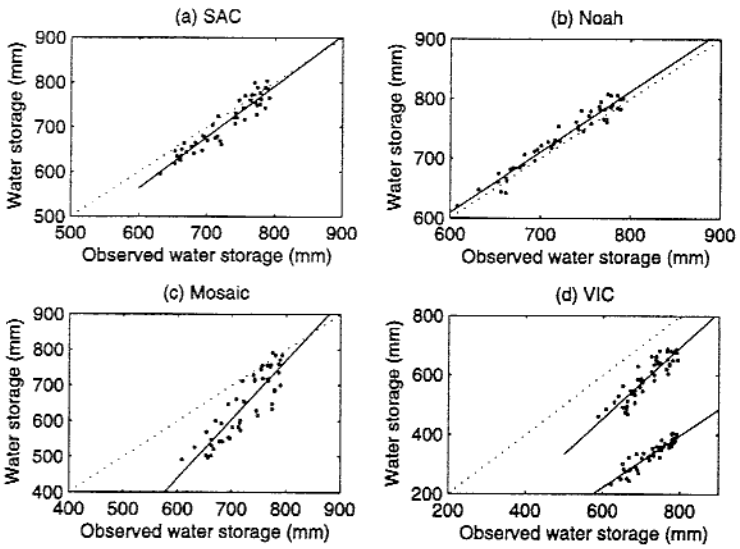

Figure 3.19. Comparison of simulated total water storage (mm) from four land surface schemes with bimonthly observations averaged over 17 locations in Illinois. The schemes are (a) SAC, (b) Noah, (c) Mosaic, and (d) VIC. From Schaake *et al.* (2004).

of soil moisture that are needed for accurate numerical weather prediction. These model results also suggest that some users may find the model predictions valuable if they are most concerned with large river basins.

To examine how well land surface schemes can reproduce local measurements of soil moisture, Liang *et al.* (1996) compare one year of weekly soil moisture measurements from a single location against results from VIC and find promising results. Crawford *et al.* (2000) use the Soil Hydrology Model (SHM; Capehart and Carlson 1994, 1997) to compare simulated soil moisture values against daily average observations of soil moisture at four depths at 38 Oklahoma Mesonet sites during July 1997. Results suggest that the SHM is able to simulate changes in soil moisture at the 5 cm level, whereas at deeper levels the model is more sluggish in responding to changes in soil moisture. They hypothesize that cracks in the soil, which form through repeated wetting and drying episodes, may be responsible for rapid increases in soil moisture at deep levels (below 50 cm) and this type of infiltration process is not represented in the SHM.

Direct comparisons between modeled soil moisture valid for a numerical model grid cell (say of 10 km × 10 km) and point soil moisture observations are a little ambiguous (Chen and Mitchell 1999; Robock *et al.* 2003), and so spatial averaging is often used to extract a more robust signal. Robock *et al.* (2003) compute daily average soil moisture observations from within the top 40 cm of soil from the Oklahoma Mesonet and compare against four land surface schemes that are again forced with the North American LDAS data. Results indicate that the land surface schemes follow the same trend as the observations (Fig. 3.20), but all the schemes clearly have biases, some of which appear to be systematic while others are related to reduced variability compared to the observations. Needless to say, obtaining accurate values of spatially averaged soil moisture is challenging, and obtaining accurate point values is even more challenging.

Part of the challenge in accurately reproducing observed soil moisture values is the heterogeneity of soil texture. Soil texture can change dramatically across very small land areas. Basara (2000) reports standard deviations approaching 10% in the silt content of soil within a small 20 m × 20 m area in central Oklahoma, similar to the differences within a single soil texture of the USDA soil texture triangle (Fig. 3.7). Robock *et al.* (2003) also compare the observed soil texture at the Oklahoma Mesonet sites to those assigned by the land surface schemes at 1/8° resolution. They find fair agreement at the 5 cm soil depth, but only rough agreement when the soil textures are integrated to get a bulk soil texture for the entire soil column (Fig. 3.21). These differences, and in particular the specification of the soil hydraulic parameters for each soil texture, play a large role in how well the land surface schemes can

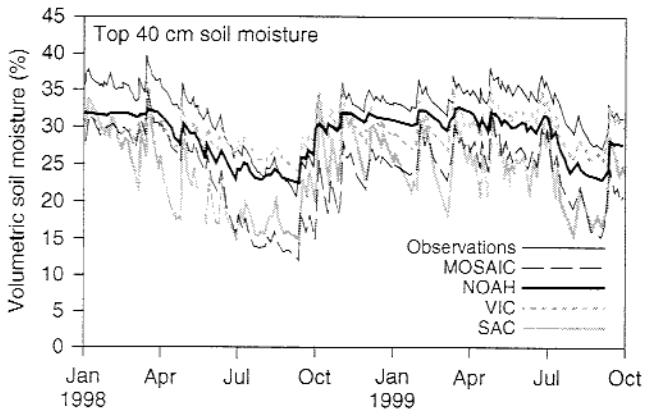

Figure 3.20. Time series from January 1998 through September 1999 of spatially and vertically averaged soil moisture in Oklahoma. Values are from observations and four land surface schemes forced by the North American LDAS. Soil moisture is for the top 40 cm layer. The schemes used are Mosaic, Noah, variable infiltration capacity (VIC), and Sacramento (SAC). Adapted from Robock *et al.* (2003).

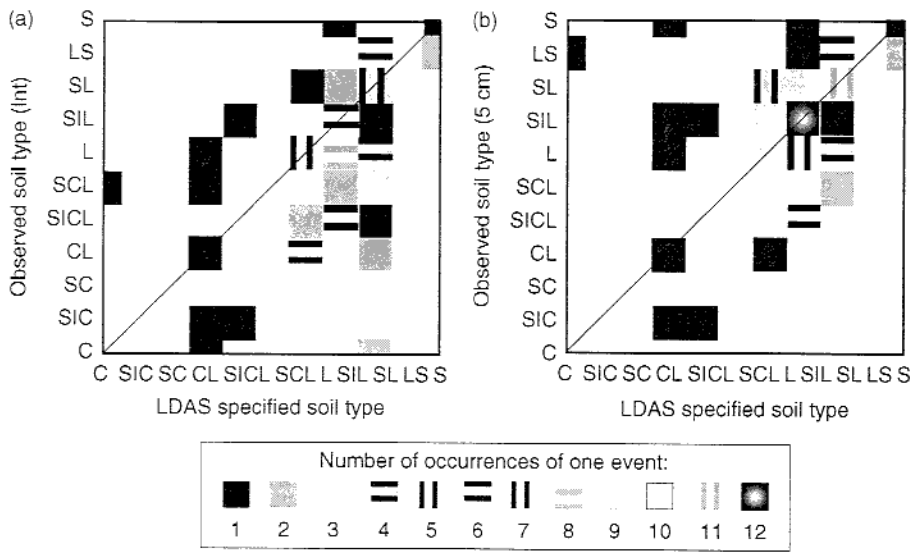

Figure 3.21. Comparison of the observed soil types at Oklahoma Mesonet stations with the land surface scheme assigned soil type at 1/8° grid spacing. Shaded squares indicate the number of occurrences of each event. A perfect correspondence between the Mesonet and assigned soil types would be indicated by a diagonal line of shaded squares. The vertical percentage values of sand, silt, and clay at the four depths at which soil moisture is observed are used to obtain a bulk soil texture for the entire column as shown in (a). The top 5 cm layer soil types are shown in (b). Adapted from Robock *et al.* (2003).

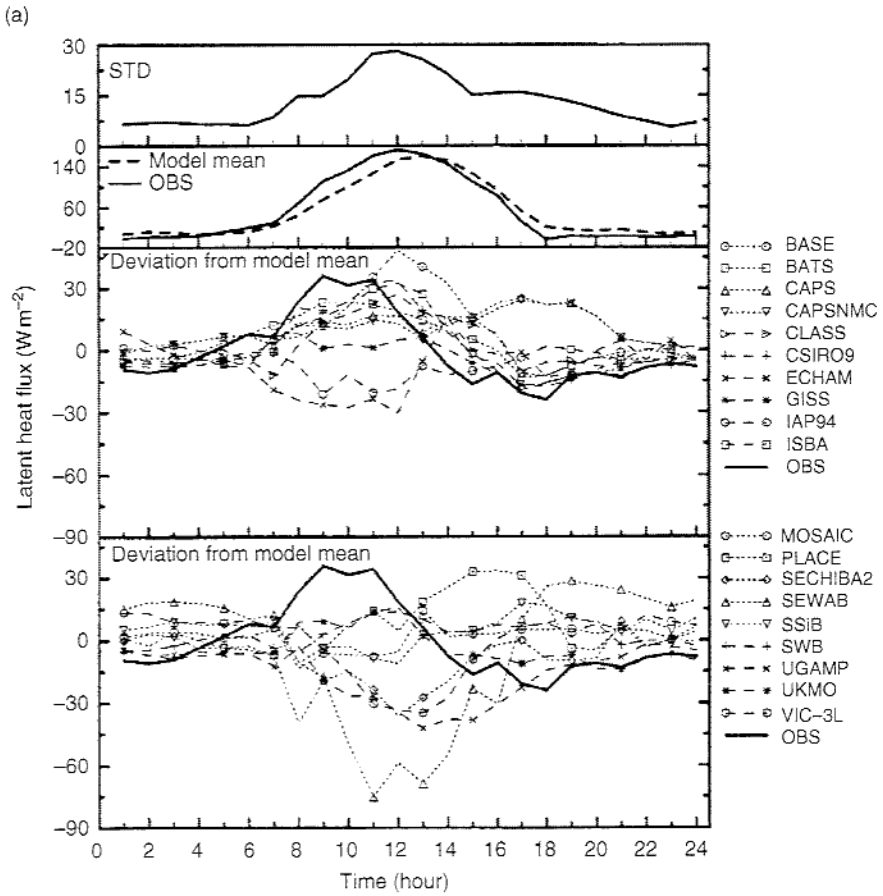

Figure 3.22. Diurnal variations of latent heat flux, sensible heat flux, and ground heat flux averaged over 10 days during September 1987 from both observations and 23 land surface schemes forced using the same input data. STD is the standard deviation of all the model values. From Chen *et al.* (1997).

reproduce the observations. In addition, Basara (2000) compares soil moisture values calculated within a 20 m × 20 m area with each other and finds coefficients of variation (standard deviation of soil moisture divided by the mean value) of over 33% in the 5 cm layer on 19 July 1999. While the values of the coefficients of variation decrease with soil depth, the variability of soil moisture within this small 400 m^2 area is large and underscores the difficulty in both trying to predict and to observe soil moisture.

One important scientific endeavor intimately related to land surface schemes is the Project for Intercomparison of Land-Surface Parameterization Schemes (PILPS; Henderson-Sellers *et al.* 1993). This project provides opportunities to compare more than 20 land surface schemes against each other and

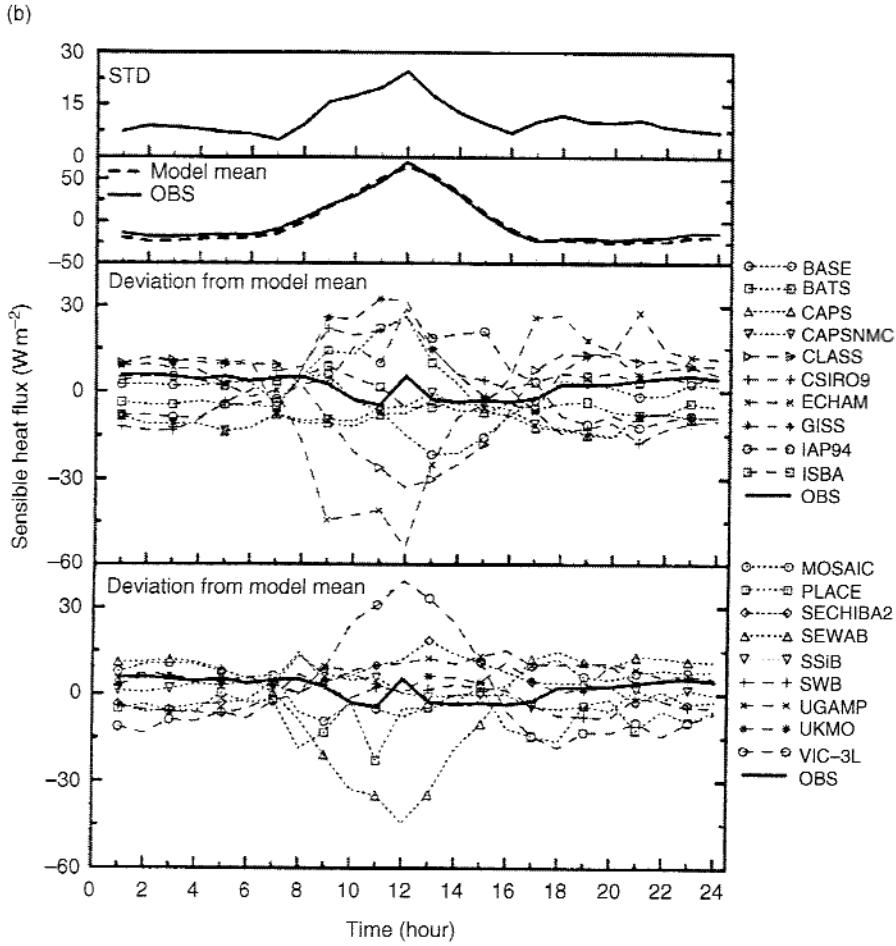

Figure 3.22. (cont.)

observations at several different locations across the globe. Results from the Cabauw, Netherlands, comparisons appear to be characteristic and indicate that there is a fairly large difference in the predicted surface fluxes from the different schemes (Fig. 3.22). The average value of all the land surface schemes differs by more than 30 W m^{-2} from observations of latent heat flux near the time of local noon, which represents a 20% error in mean flux magnitude. The average value of sensible heat flux is in much closer agreement with the observations, yet the variability from scheme to scheme remains large and represents over half of the observed flux magnitude for the days evaluated. The situation for the ground heat flux is no different, with the average value from all the schemes departing from observations by nearly 40 W m^{-2}. Similar

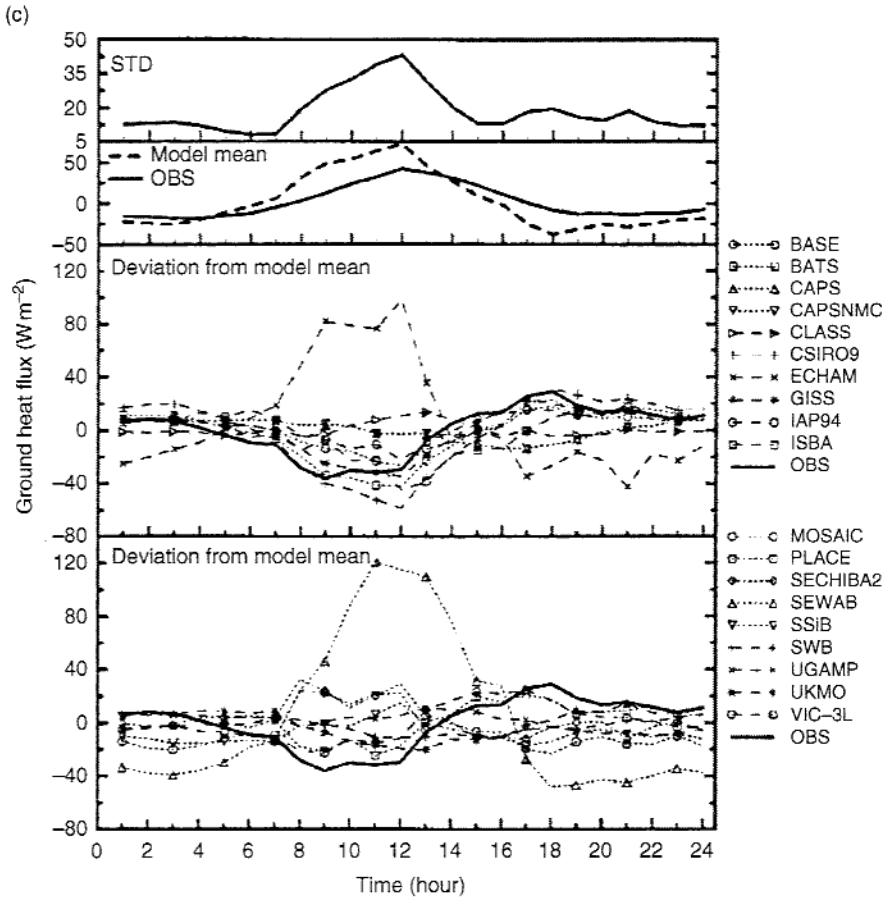

Figure 3.22. (cont.)

results are seen in Robock *et al.* (2003) for four land surface schemes that are forced using the North American LDAS and in Marshall *et al.* (2003) for the operational Eta model. These results clearly indicate that simulating or forecasting accurate surface fluxes is a very difficult challenge.

These errors in the specification of soil moisture, soil texture, vegetation fraction, and even the scheme physical process representations all lead to errors in variables that are more familiar to us and to the public. Kurkowski *et al.* (2003) compare Eta model forecasts using climatological values for the green vegetation fraction (Eta) with forecasts using near real-time satellite-derived green vegetation fraction (VegEta). Results show that the use of near real-time satellite-derived vegetation fraction leads to differences approaching 1 °C for midday 2 m temperatures and exceeding 2 °C for midday dewpoint temperatures (Fig. 3.23) and leads to reduced errors in these predicted values.

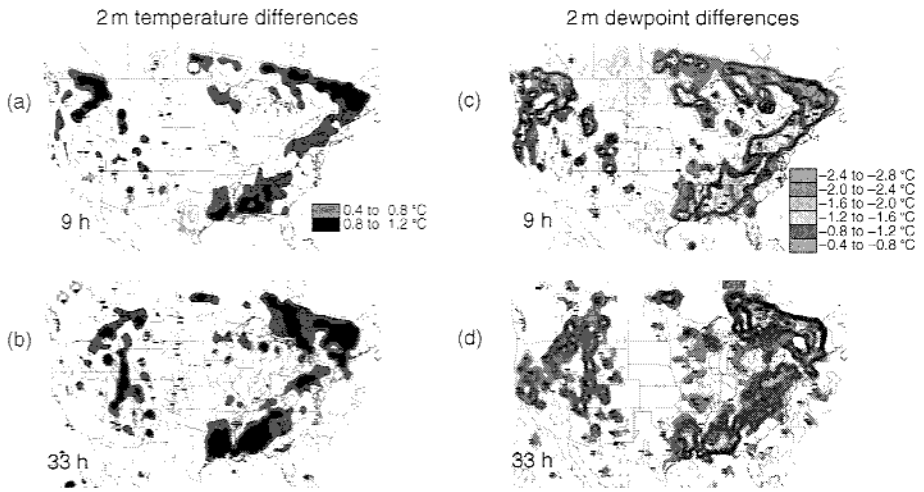

Figure 3.23. Differences in 2 m temperatures from two Eta model forecasts from 13 May 2001 at the (a) 9 h and (b) 33 h forecast times (2100 UTC). Differences are defined as Eta model using satellite-derived vegetation fraction minus Eta model using climatological vegetation fraction, and the isolines are every 0.2 K. Keys highlight the color schemes used for the various difference values. From Kurkowski *et al.* (2003).

This effect is seen more clearly early during the growing season, when vegetation departures from climatology appear to be larger and more likely to persist (Fig. 3.24). These results highlight that improvements in our specification of land surface characteristics lead directly to improvements in model forecasts.

These results all strongly suggest that the accurate specification of the land surface, in terms of soil and vegetation properties, is an important and timely issue for the meteorological community. It is clear that the addition of improved data leads to improved forecasts, even with land surface schemes that are far from perfect. This only makes sense, as we have seen how additional data have improved our atmospheric models for decades. For land surface schemes, initial data to truly specify the state of the land and vegetation surface at the model initial time are few and far between. Most are based upon using climatological data or calculations from land data assimilation systems. While these systems are significant improvements over what was available in the past, they also are not equivalent to having actual observations. Efforts to improve this situation are certain to yield good results and help the meteorological community in general to provide better services to the public.

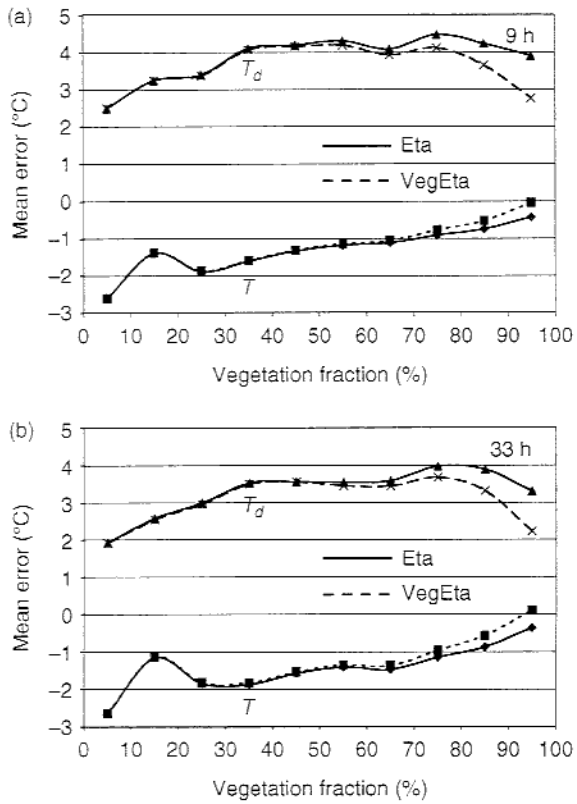

Figure 3.24. Mean temperature (T) and dewpoint temperature (T_d) errors vs. satellite-derived vegetation fraction for 12 cases of Eta model forecasts for (a) 9 h and (b) 33 h forecast times (both 2100 UTC). Solid lines are for the Eta forecasts and dashed lines are for the Eta forecasts with the satellite-derived vegetation fraction (VegEta). Data are averaged over 10% vegetation fraction bins. From Kurkowski *et al.* (2003).

3.10 Questions

1. The following data were taken over a tall grass field at Norman, Oklahoma on 17 May 2004 at local noon.

IR surface temperature	37 °C
Air temperature	28 °C at 2 m
Specific humidity of air	14 g kg^{-1} at 2 m
Wind speed	7.0 m s^{-1} at 10 m
Vegetation height	1.0 m
Leaf area index	2.0
Net radiation	600 W m^{-2}
Ground heat flux	100 W m^{-2}

Rainfall totals of slightly more than 0.25 in occurred the day before.

(a) Calculate the sensible heat flux, assuming neutral stability for the log profile laws. Using the surface energy balance and the calculated sensible heat flux, solve for the evapotranspiration flux.

(b) Calculate the Monin–Obukhov length using the value of u_* calculated above. Note that Stull (1988) shows that

$$\overline{w'\theta_v'} = \overline{w'\theta'}(1 + 0.61\bar{q}) + 0.61\bar{\theta}(\overline{w'q'}).$$

(c) Recalculate the value of u_* for non-neutral conditions. How much does it change from the value determined for neutral conditions? Recalculate the sensible heat flux, and note how much it changes. How much would u_* have to change to alter the sensible heat flux by $50\,\mathrm{W\,m^{-2}}$?

2. Using the same data as in Question 1, examine the calculations for bare soil evaporation when the green vegetation fraction is zero. Assume that the Richardson number is zero, $\Theta_1 = 0.35$, $\Theta_{fc} = 0.45$, and $\Theta_w = 0.18$. Use (3.6) and (3.7) to calculate bare soil evaporation. Then use (3.8) and (3.9) instead to calculate bare soil evaporation. Comment on the differences in the calculated fluxes.
3. Again, using the same data as in Question 1, examine the calculations for evapotranspiration from vegetation when the vegetation fraction is 1. Assume that the Richardson number is zero, $\Theta_1 = 0.35$, $\Theta_2 = 0.25$, $\Theta_{fc} = 0.45$, and $\Theta_w = 0.18$. The first soil layer is 10 cm deep, and the second soil layer that incorporates the rest of the root zone is 40 cm deep. Assume that $W_c = 0$, so that the canopy surface is dry. Use (3.24) and (3.25) to calculate the evapotranspiration. If one further assumes that $Q_S = 700\,\mathrm{W\,m^{-2}}$, $Q_{GL} = 50\,\mathrm{W\,m^{-2}}$, $r_{c\,min} = 100\,\mathrm{s\,m^{-1}}$, and $\alpha = 40$ in the definition of F_2, then use (3.38)–(3.43) to calculate evapotranspiration assuming $r_r = 15\,\mathrm{s\,m^{-1}}$. Comment on the differences in the calculated fluxes.
4. sing the same data as in Question 1 and the results of Questions 2 and 3, calculate the total latent heat flux as a function of the vegetation fraction as the vegetation fraction varies from 0 to 1 in increments of 0.1. If one assumes that errors of 10% in vegetation fraction are reasonable, how large is the uncertainty in the latent heat flux?
5. For a 50% vegetation fraction at a particular grid cell, assume errors of 10% in the vegetation fraction and errors of $0.05\,\mathrm{m^3\,m^{-3}}$ in volumetric soil moisture measurements. Using (3.6) and (3.7) for the bare soil evaporation and (3.24) and (3.25) for evapotranspiration from the vegetation, determine the range in uncertainty for the total latent heat flux owing to these two factors. Comment on the importance of these two measurements.
6. Calculate the values of soil potential for sand, loam, and sandy clay from $\Theta = 0.05$–0.40 with $\Theta_s = 0.40$ assumed for all three soil textures. Assume that $\kappa_s = 1 \times 10^{-5}\,\mathrm{m\,s^{-1}}$ and that $\psi_s = -0.5\,\mathrm{J\,kg^{-1}}$. Using the results in Table 3.1, incorporate one standard deviation in the values of b and recalculate the values of soil potential. Using (3.69), calculate the values of diffusivity D for these nine values of soil potential. Comment.

7. Using the same basic data as in Question 1, examine the benefits of mosaic tiling. The latent heat flux for 1 m tall grasses has already been calculated. Now assume that 70% of the model grid cell is represented by these grasses, but that 30% of the model grid cell is represented by oak trees that are 8 m tall and have a LAI of 10. Determine the latent heat flux using the tiling approach of (3.46). Comment on the differences in the values of latent heat flux for a homogeneous versus heterogeneous land surface as described.